The Astrophysical Journal Supplement Series, 279:33 (15pp), 2025 August https://doi.org/10.3847/1538-4365/addf4f


# Revisiting the Dynamical Model for the Evolution of Hot Spots and Its Cosmological Application

Yalong Nan[1,2], Shuo Cao[1,2], Tao An[3,4], Haiyan Zhang[5,6], Wuzheng Guo[1,2], Ailing Zeng[7], Shiming Wen[4], and Ruobing Ding[1,2]

[1] Institute for Frontiers in Astronomy and Astrophysics, Beijing Normal University, Beijing 102206, People's Republic of China; caoshuo@bnu.edu.cn
[2] School of Physics and Astronomy, Beijing Normal University, Beijing 100875, People's Republic of China
[3] Shanghai Astronomical Observatory, Chinese Academy of Sciences, Shanghai 200030, People's Republic of China; antao@shao.ac.cn
[4] Xinjiang Astronomical Observatory, CAS, 150 Science 1-Street, Urumqi, Xinjiang 830011, People's Republic of China
[5] National Astronomical Observatories, Chinese Academy of Sciences, Beijing 100101, People's Republic of China; hyzhang@bao.ac.cn
[6] Key Laboratory of Radio Astronomy and Technology, National Astronomical Observatories, Chinese Academy of Sciences, Beijing 100101, People's Republic of China
[7] Instituto de Astrofísica de Andalucía, Gta. de la Astronomía, s/n, Genil, 18008 Granada, Spain
*Received 2024 December 1; revised 2025 May 13; accepted 2025 May 30; published 2025 July 14*

## Abstract

Compact symmetric objects (CSOs) typically refer to small-scale extragalactic radio sources (usually <1 kpc) that exhibit strong radio emission on both sides (hot spots) and have a symmetric morphology. In this paper, we revisit the dynamical model for the evolution of hot spots in powerful radio sources, based on the latest bona fide CSO sample with well-defined statistical characteristics. Specifically, we focus on the subsample of CSOs that exhibit edge brightening, high luminosity, and prominent hot spots, and furthermore derive their luminosity and linear sizes between tens to hundreds of parsecs. The luminosity–linear size relation highlights the significant potential of CSOs in the study of modern cosmology. Finally, we investigate the possibility of testing the dynamical hot spot model with a much higher accuracy using CSOs observed in future very long baseline interferometry surveys. It is shown that our method could provide an independent test of the cosmic distance duality relation, reinforcing the potential of CSOs acting as a reliable cosmological probe.

*Unified Astronomy Thesaurus concepts:* Radio active galactic nuclei (2134); Radio hot spots (1344); Observational cosmology (1146)

## 1. Introduction

Active galactic nuclei (AGNs) are the cores of galaxies that exhibit intense activity and complex physical processes (C. M. Urry & P. Padovani 1995), characterized by an extremely high luminosity observable even at very high redshifts. Some AGNs show prominent jet structures with scales ranging from parsecs to megaparsecs. These jets serve as cosmic "rulers" whose evolution encodes information about both the local physics of AGN and the global properties of spacetime through which they propagate (R. Blandford et al. 2019). With the continuous advancement in the spatial resolution of radio telescopes, it has become possible to study these jets at various scales in detail. Among AGN populations, compact symmetric objects (CSOs) present a particularly valuable subset, which is characterized by compact symmetric radio morphology with total size <1 kpc, well-defined hot spots marking the jet termination, minimal relativistic beaming effects, and systematic evolution in their luminosity–size relation (hereafter *P–D* relation) (P. Wilkinson et al. 1994; A. Readhead et al. 1978; T. An & W. A. Baan 2012). This lack of significant beaming is crucial (A. Readhead et al. 1993; P. Wilkinson et al. 1994), as it allows more reliable intrinsic luminosity estimates compared to highly beamed sources like blazars.

Due to the lack of observational data and the inability to quantify the beaming effect, limitations exist in the current CSO sample. Although many early studies aimed to construct a purer CSO sample, increasing observational evidence suggests that many CSO candidates are better suited to be classified as core-jet sources. To address this issue, S. Kiehlmann et al. (2024) proposed incorporating flux variability and apparent velocity as additional selection criteria alongside traditional morphological criteria. Based on these refined criteria, they developed a sample of 79 bona fide CSOs. However, due to insufficient observational data, the variability indices and line-of-sight velocities could not be comprehensively applied to all sources in the sample. Hot spots, formed by the interaction between jets and the surrounding interstellar medium, are typically considered the endpoints of jets and are characterized by their dense morphology and high brightness. Recent magnetohydrodynamic simulations (D. L. Meier 2012; M. Nakamura et al. 2018; M. Perucho et al. 2019) and high-resolution very long baseline interferometry (VLBI) observations have revealed sophisticated physics in these regions, including magnetic field amplification through compression, complex particle acceleration processes, and interaction with multiphase ambient media. The properties of these hot spots provide multiple independent methods to estimate the kinematic age of CSOs, through direct proper-motion measurements (G. B. Taylor et al. 2000; A. G. Polatidis & J. Conway 2003; H. Nagai et al. 2006; T. An et al. 2011; T. An & W. A. Baan 2012), and radiative age based on spectral break analysis from synchrotron cooling (N. S. Kardashev 1962; M. Murgia et al. 2002; M. Murgia 2003; H. Nagai et al. 2006).

The convergence of these different age indicators strongly supports the youth scenario for a fraction of CSOs.

Fundamental tests of cosmological principles require diverse and independent observational probes. While Type Ia supernovae (SNe Ia) and baryon acoustic oscillations (BAOs) have traditionally served as primary distance indicators, the field urgently needs new probes to bridge different cosmic distance measures. Numerous studies have demonstrated the significant potential of compact radio sources in cosmology, particularly for testing the angular size–redshift relation, which can serve as "standard rulers" to provide angular diameter distances in a cosmology-model-independent way (K. I. Kellermann 1993; L. Gurvits 1994; L. Gurvits et al. 1999). Notably, S. Cao et al. (2015, 2017a) introduced a sample of intermediate-luminosity flat-spectrum radio quasars, whose linear size shows minimal dependence on luminosity and redshift across a wide redshift range. This sample significantly extends the redshift coverage beyond that of BAO and SNe Ia, especially at higher redshifts, enabling the exploration of various cosmological topics, such as the dynamic evolution of dark energy (S. Cao et al. 2017b), high-redshift tests of the cosmic distance duality relation (CDDR; J.-Z. Qi et al. 2019b; X. Zheng et al. 2020; T. Liu et al. 2021), and measurements of cosmic curvature (S. Cao et al. 2019; J.-Z. Qi et al. 2019a, 2021). Furthermore, CSOs follow well-defined evolutionary tracks in the luminosity–size diagram. The interpretation of systematic trends in their luminosity–size evolution (M. Kunert-Bajraszewska et al. 2010; T. An & W. A. Baan 2012; M. Hardcastle & J. Croston 2020; C. P. O'Dea & D. Saikia 2021) is crucial for understanding the growth and evolution of radio galaxies. This relation also provides a potential route to standardize CSOs as cosmological distance indicators, particularly for testing the CDDR—a fundamental pillar of observational cosmology. This relation, which links the luminosity distance $D_L(z)$ with the angular diameter distance $D_A(z)$ at redshift $z$, relies on photon number conservation and light propagation along geodesics in a Riemannian spacetime (I. M. H. Etherington 1933). Therefore, the possible deviation from the CDDR could indicate the existence of new physics or systematics in observations (S. Cao & Z. Zhu 2011; S. Cao et al. 2016). The $P$–$D$ relation of CSOs provides information on both angular diameter distance and luminosity distance, thus naturally serving as a new test for the CDDR.

In this paper, we aim to refine the theoretical understanding of CSO evolution through improved hot spot dynamics modeling, establish CSOs as reliable cosmological probes through rigorous statistical analysis, and test fundamental cosmological relations using a novel class of standardizable objects. The paper is organized as follows: Section 2 presents our refined theoretical model of CSO evolution. Section 3 details the current observational data and the corresponding statistical analysis. Section 4 explores the data simulation and its cosmological applications, particularly for the CDDR testing. Finally, we summarize the main conclusions in Section 5.

## 2. Theoretical Model of CSO Evolution

The evolution of radio-loud AGN represents a fundamental challenge in astrophysics, requiring a unified framework that connects microscale jet physics to macroscale source evolution. CSOs provide an ideal laboratory for studying this connection, as their evolution can be tracked through multi-epoch VLBI observations. Despite the selection effect, more evidence tends to suggest that a fraction of the CSO population is a type of young radio source that may evolve into large-scale double radio sources. Therefore, describing the evolution of CSOs is crucial for understanding the jet and accretion processes in AGN. These features demand a theoretical framework that can self-consistently explain both their internal physics and evolutionary behavior.

Most theories of CSO evolution rely on the minimum energy assumption, where the magnetic field and particle energy reach approximate equilibrium. Moreover, radio emissions are primarily produced by synchrotron radiation. Recent relativistic magnetohydrodynamic simulations by M. Perucho et al. (2019) have validated this assumption, showing that magnetic field amplification in hot spots naturally drives systems toward equipartition through compression and turbulence on timescales much shorter than the source lifetime.

The theoretical description of CSO evolution has progressed through several key stages. A. Readhead et al. (1996) assumed ram pressure equilibrium between the jets and external medium, investigating the evolution of CSOs under constant power, with a focus on the relationship between hot spot advance speed and luminosity. C. P. O'Dea & S. A. Baum (1997) further proposed a connection between the evolution of CSOs and large-scale double radio sources (FR II), establishing the theoretical foundation for CSOs as precursors to large radio sources. The studies by C. Fanti et al. (1995) and I. Snellen et al. (2000) introduced the self-similar evolution hypothesis for CSOs, thoroughly exploring the relationship between radio luminosity and linear size. Building on this, J. Carvalho (1994), J. C. Carvalho (1998), and M. C. Begelman (1996) further analyzed jet behavior in the external medium, with particular attention to the effects of external density gradients on jet propagation. Based on these works, M. Perucho & J. Martí (2003) developed a more sophisticated model that incorporates time-dependent jet power and environmental effects, which forms the basis of our analysis.

In this paper, we utilize the dynamical hot spot model proposed by M. Perucho & J. Martí (2003), which describes the time-varying physical properties of CSOs. The model's key innovation is its treatment of jet power $Q_{\rm j}$ and hot spot radius $r_{\rm hs}$ as functions of time: $r_{\rm hs} \propto t^{\beta}$ and $Q_{\rm j} \propto t^{\epsilon}$, following power-law evolution as the source expands, where $\beta$ and $\epsilon$ are physically motivated parameters reflecting the coupling between jet dynamics and environmental interaction. The model also describes the density profile of the external medium, assuming it varies with the CSOs' linear size as $\rho_{\rm ext} \propto ({\rm LS})^{-\delta}$. This power-law form is supported by X-ray observations of CSO host galaxies (O. Tengstrand et al. 2009; A. Siemiginowska et al. 2016), which reveal systematic density gradients in the circumnuclear regions.

Due to the ram pressure equilibrium, the hot spot velocity $v_{\rm hs}$ can be written as

$$v_{\rm hs} = \sqrt{\frac{F_{\rm j}}{A_{\rm j,hs}\rho_{\rm ext}}}, \tag{1}$$

where $F_{\rm j}$ is the jet thrust, which can be calculated as $F_{\rm j} \approx Q_{\rm j}/c$, while $A_{\rm j,hs}$ denotes the cross-sectional area of the jet. This relation follows the conservation of momentum flux in relativistic jets (M. C. Begelman et al. 1984; C. R. Kaiser &

P. Alexander 1997) and represents a first-order approximation of jet propagation models. However, it is important to note that this approximation may need modification when strong magnetic fields are present. Substituting the definitions of $Q_j$, $r_{hs}$, and linear size into Equation (1) and performing the integration, $t$ can be expressed as a function of linear size, with both $r_{hs}$ and $v_{hs}$ subsequently written as functions of linear size. The next equation in this model comes from the source energy balance, i.e., the power consumed by the source in the hot spot advance, adjusts to the evolution of the jet kinetic power

$$(P\dot{d}V)_{hs,adv} \propto (P_{hs} r_{hs}^2 v_{hs}) \propto Q_j \propto t^{\epsilon}, \quad (2)$$

where $P_{hs}$ is the pressure of the cocoon. The cocoon originates from the interaction between the jet and the ambient medium, where the material deflected from the reverse shock accumulates and surrounds the jet. Under the assumption of minimum energy, the luminosity of the hot spot can be written as $L_{hs} \propto P_{hs}^{7/4} r_{hs}^3$. Therefore, the luminosity is also a function of time and linear size. Similar to the previous discussion, time can be expressed as a function of linear size, making the luminosity a single-valued function of linear size.

## 3. Observations and Data Analysis

The sample used in this study was selected by S. Kiehlmann et al. (2024). Except for the previous morphological analysis, the authors also constrained the variability and apparent velocity to eliminate contamination in the CSO population, which are often overlooked in previous works. Using these criteria, S. Kiehlmann et al. (2024) identified 79 bona fide CSOs. S. Tremblay et al. (2016) conducted a comprehensive survey of CSOs to date and discovered that CSOs can be divided into two classes, similar to the classification of FR I and FR II radio galaxies (B. L. Fanaroff & J. M. Riley 1974). The first class is characterized by edge-dimmed, low-luminosity features, and is designed as CSO1; while the other class is characterized by edge-brightened, high-luminosity features, and is designed as CSO2. CSO2 can be further divided into three categories: CSO2.0, with prominent hot spots and narrow jets; CSO2.2, lacking hot spots but with broad jets; and CSO2.1, combining characteristics of the other two. These classifications allowed A. G. Sullivan et al. (2024) to explore the various morphologies and evolutionary processes of CSOs in detail. For the purposes of testing the dynamic model of hot spots, we only select CSO2.0s.

To quantify the flux density and linear size of CSOs within the same frequency band, we utilize publicly available *S*- and *X*-band images of these sources, with additional *C*-band and *U*-band data for some cases. This multifrequency approach is crucial for constraining spectral properties, investigating frequency-dependent effects, and mitigating resolution-dependent biases in our analysis. We download *uv* data from the Astrogeo VLBI database[8] and perform model fitting on the *uv*-plane using the DIFMAP software (M. Shepherd et al. 1994). The uncertainties in the fitting parameters are calculated following the methodology of K. Sokolovsky et al. (2011) and S.-S. Lee et al. (2008). This comprehensive approach accounts for thermal noise in the visibility measurements, systematic calibration uncertainties, and complex source structure effects. After model fitting, we derive the spectral index between bands by assuming a power-law spectrum ($S \propto \nu^{\alpha}$). Then these quantities are used to calculate the luminosity by using $L = 4\pi D_L^2 S(1+z)^{\alpha-1}$ (T. An & W. A. Baan 2012), where $D_L$ is the luminosity distance and $z$ is the redshift. This formulation properly accounts for both K-correction and cosmological effects. However, it should be emphasized that the calculation of luminosity also depends on the choice of specific cosmological parameters.

Converting the observed quantities to intrinsic physical quantities of CSOs requires the distance information at the source redshift $z$. Over the past few decades, considerable advances have been made in developing two classes of probes that may be used to observe cosmological distances. Luminous sources of known (or standardizable) luminosity such as SNe Ia (F. Hoyle & W. A. Fowler 1960; D. Branch & G. Tammann 1992; M. M. Phillips 1993), UV and X-ray quasars (G. Risaliti & E. Lusso 2015, 2019) can serve as standard candles, providing the measurements of luminosity distances. In order to measure the angular diameter distances, one can always turn to objects of known (or standardizable) comoving size acting as "standard rulers" in the Universe. BAO (E. E. Ishida et al. 2008; R. Lazkoz et al. 2008; L. Samushia & B. Ratra 2009), galaxy clusters (E. De Filippis et al. 2005; M. Bonamente et al. 2006), compact radio quasars (S. Cao et al. 2017a, 2017b) are often adopted to provide standard rulers under certain assumptions. In this paper, we use the Pantheon+SH0ES data set consisting of 1701 light-curve measurements from 1550 distinct SNe Ia ranging in redshift from $z = 0.001$ to 2.26 (D. Brout et al. 2022; A. G. Riess et al. 2022). More specifically, the calibrated distance modules of each SNe Ia can be calculated as

$$\mu(z) = m_B - M_B = 5\log\left(\frac{D_L(z)}{\mathrm{Mpc}}\right) + 25, \quad (3)$$

where $m_B$ and $M_B$ represent the apparent and absolute magnitude in $B$ band, while $D_L(z)$ is the luminosity distance at redshift $z$. Considering that the number of data and the uniformity of the spaced data will strongly affect CSO calibration, we use the publicly available code (M. Seikel et al. 2012) called Gaussian processes in Python (GaPP) to reconstruct the luminosity distance at different redshifts. The reconstructed $D_L(z)$ results are shown in Figure 1. Note that the angular diameter distance can be directly derived from the CDDR: $D_A(z) = D_L(z)/(1+z)^2$ (I. M. H. Etherington 1933). Based on the reconstructed $D_L(z)$ with the validity of CDDR, we can estimate the intrinsic physical quantities of the CSOs (hereafter Sample I), with the results summarized in Table 1.

Note that although using the Pantheon+SH0ES SNe Ia data to calibrate the CSO2.0 sample does not rely on a specific cosmological model, the validity of the CDDR is still assumed. We can also measure the $D_A(z)$ by using the Sunyaev–Zeldovich effect together with X-ray emission of 25 galaxy clusters (E. De Filippis et al. 2005). Similarly, we use GaPP to reconstruct the redshift—angular diameter distance relation, with the reconstructed results shown in Figure 1. Due to the limited redshift range of the cluster sample, we can only calibrate 11 low-redshift sources in the CSO2.0 sample, with the redshift range $z < 0.8$ (hereafter Sample II).

[8] https://astrogeo.org/vlbi_images/

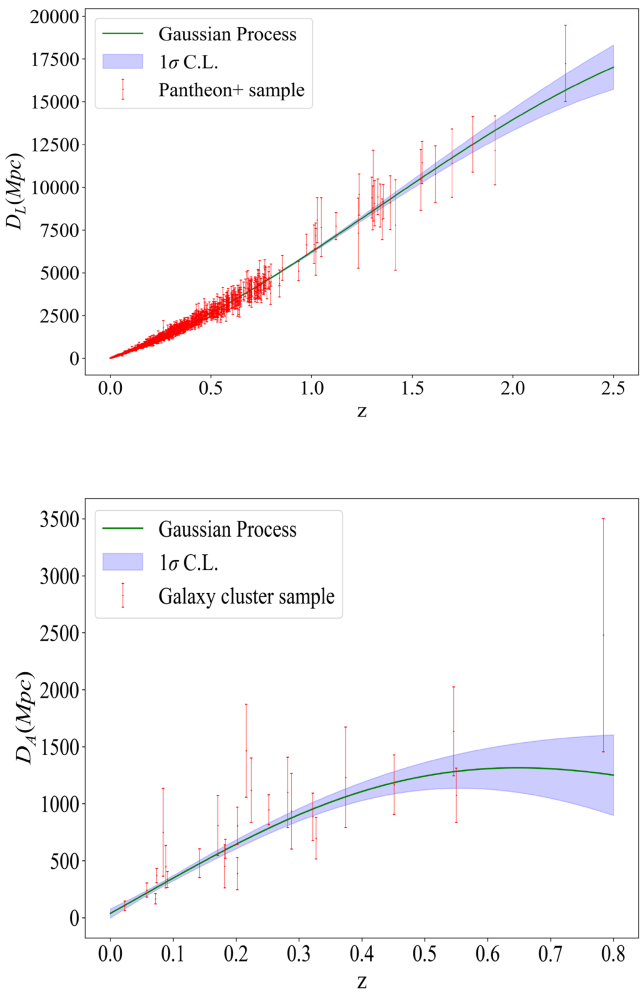


**Figure 1.** Upper panel: Gaussian process reconstructed $D_L(z)$ using the Pantheon+SH0ES SNe Ia sample (D. Brout et al. 2022; A. G. Riess et al. 2022). Lower panel: Gaussian process reconstructed $D_A(z)$ using the galaxy cluster sample (E. De Filippis et al. 2005).

To minimize the impact of differing resolutions across bands, we implement a robust cross-frequency analysis strategy. Our approach involves restricting model fitting to the *uv*-range common to both *S*- and *X*-band data, using consistent component models across frequencies, and applying resolution-matched filtering (K. Sokolovsky et al. 2011). This careful treatment ensures that our multifrequency comparisons are not biased by resolution-dependent effects. We use the least squares method to fit the relationships between luminosity, hot spot radius, and the linear size of CSOs. The best fits and the corresponding uncertainties of the hot spot parameters, based on different CSO samples, are summarized in Table 2. The error regions shown in Figures 2 and 3 are calculated through the well-known standard error propagation method, accounting for the uncertainties in the fitted parameters.

As discussed in Section 2, the hot spot radius, velocity, and luminosity can all be expressed as functions of the linear size of CSO. Their power-law indices are denoted as $s_r$, $s_v$, and $s_L$. The relationships between these indices and the three main parameters of the model, $\beta$, $\delta$, and $\epsilon$, are governed by a set of coupled equations that emerge from the self-similar evolution assumption and conservation laws (C. R. Kaiser & P. Alexander 1997)

$$\beta = \frac{s_r}{1 - s_v}, \tag{4}$$

$$\delta = \frac{12}{7}s_r - \frac{4}{7}s_L + s_v, \tag{5}$$

$$\epsilon = \frac{\frac{2}{7}s_r + \frac{4}{7}s_L + s_v}{1 - s_v}. \tag{6}$$

In this paper, although we do not directly calculate the velocity of the hot spot, we are able to analyze nine high-power CSOs with known hot spot velocity (T. An & W. A. Baan 2012). We perform a least squares fit, and the results are also presented in Figure 2. These measurements provide crucial validation of our theoretical framework and offer independent constraints on the model parameters. The variation in hot spot velocity with linear size follows an approximate power-law relation, with an exponent of $0.53 \pm 0.148$. Previous studies suggested that for CSOs with constant luminosity, the hot spot velocity decreases with increasing linear size. The positive correlation we observe suggests that more powerful jets, which typically drive faster hot spot advancement, also tend to create larger-scale structures more rapidly. This observation provides strong support for self-similar evolution models of radio source development. By combining the $s_r$ and $s_L$ values in Table 2, we can derive the three parameters of the hot spot dynamical model (Sample I): $\beta = 0.924 \pm 0.493$, $\epsilon = 3.075 \pm 1.412$, and $\delta = 0.487 \pm 0.441$. The value of $\delta$ is smaller than 1 adopted by A. G. Sullivan et al. (2024) in the simulation. For Sample II, the parameters of the hot spot dynamical model change to $\beta = 1.470 \pm 0.570$, $\epsilon = 3.534 \pm 1.581$, and $\delta = 0.785 \pm 0.435$, which are well consistent with those derived from Sample I within $1\sigma$ confidence limit (C.L.). However, the parameter $\delta$, which is slightly larger than that from Sample I, agrees very well with the simulation results within $1\sigma$ C.L. Such differences suggest that the density profile of the environment may be related to the redshift, which has important implications for understanding the interaction between young radio sources and their host galaxies.

Meanwhile, we utilize the dual-band data, and for certain sources, publicly available data across three or four bands to calculate variations in linear size at different frequencies. It is found that the linear size tends to increase at higher frequencies, as shown in Figure 4 and Table 3. K. Sokolovsky et al. (2011) proposed that such a difference cannot be explained solely by resolution differences. Furthermore, they pointed out that when the jet crosses the hot spots, it deflects and forms a backflow. In this backflow, high-energy particles cool faster, resulting in high-frequency emission being concentrated closer to the hot spots, while low-energy particles cool more slowly, causing low-frequency emission to appear closer to the core. They employed the SPEV code (P. Mimica et al. 2010) to simulate the differences in CSO separation scales at *S* and *X* bands but failed to reproduce the observed magnitude of the difference. They noted that more detailed modeling, which fully accounts for synchrotron opacity effects, and dedicated simultaneous multifrequency VLBI observations are likely necessary to determine the exact origin of the positional differences of the hot spots.

## 4. Data Simulation and Its Cosmological Application

Given the limited sample size, which brings significant statistical uncertainties for model fitting, we refer to the

**Table 1**
CSO2.0 Sample from S. Kiehlmann et al. (2024)

| J2000 ID | $z$ | Band | Obs Date | Luminosity (W Hz$^{-1}$) | Linear Size (pc) | $r_{hs}$ (pc) | References |
|---|---|---|---|---|---|---|---|
| J0029+3456 | 0.517 | *S* | 1996/05/15 | $(1.083 \pm 0.219) \times 10^{27}$ | $168.316 \pm 4.328$ | $17.617 \pm 2.948$ | A. Beasley et al. (2002) |
| | | *C* | 1996/06/05 | $(8.951 \pm 2.255) \times 10^{26}$ | $170.439 \pm 6.071$ | $15.989 \pm 4.021$ | E. Fomalont et al. (2000) |
| | | *X* | 1996/05/15 | $(5.911 \pm 1.780) \times 10^{26}$ | $166.879 \pm 6.957$ | $14.408 \pm 4.702$ | A. Beasley et al. (2002) |
| | | *U* | 1996/07/10 | $(2.048 \pm 0.460) \times 10^{26}$ | $176.798 \pm 2.708$ | $5.126 \pm 1.339$ | M. Lister et al. (2009) |
| J0111+3906 | 0.66847 | *S* | 1996/06/07 | $(1.254 \pm 0.115) \times 10^{27}$ | $35.531 \pm 0.966$ | $9.774 \pm 0.669$ | A. Beasley et al. (2002) |
| | | *C* | 1996/06/05 | $(1.585 \pm 0.220) \times 10^{27}$ | $34.844 \pm 1.244$ | $7.782 \pm 0.859$ | E. Fomalont et al. (2000) |
| | | *X* | 1996/06/07 | $(9.992 \pm 2.096) \times 10^{26}$ | $35.857 \pm 1.712$ | $6.979 \pm 1.186$ | A. Beasley et al. (2002) |
| | | *U* | 1997/02/03 | $(4.378 \pm 0.572) \times 10^{26}$ | $37.345 \pm 0.629$ | $3.517 \pm 0.351$ | M. Lister et al. (2009) |
| J0405+3803 | 0.05505 | *S* | 1996/06/07 | $(6.917 \pm 1.224) \times 10^{24}$ | $32.081 \pm 0.760$ | $3.782 \pm 0.515$ | A. Beasley et al. (2002) |
| | | *C* | 1996/06/05 | $(4.096 \pm 0.860) \times 10^{24}$ | $32.051 \pm 1.444$ | $3.521 \pm 0.884$ | E. Fomalont et al. (2000) |
| | | *X* | 1996/06/07 | $(3.213 \pm 0.813) \times 10^{24}$ | $32.845 \pm 0.866$ | $2.007 \pm 0.569$ | A. Beasley et al. (2002) |
| J0713+4349 | 0.518 | *S* | 1996/06/07 | $(2.106 \pm 0.372) \times 10^{27}$ | $137.286 \pm 2.342$ | $10.625 \pm 1.596$ | A. Beasley et al. (2002) |
| | | *C* | 1996/06/05 | $(1.221 \pm 0.238) \times 10^{27}$ | $140.638 \pm 1.117$ | $6.963 \pm 0.339$ | E. Fomalont et al. (2000) |
| | | *X* | 1996/06/07 | $(7.156 \pm 1.730) \times 10^{26}$ | $140.592 \pm 2.301$ | $5.170 \pm 1.476$ | A. Beasley et al. (2002) |
| J0943+1702 | 1.60115 | *S* | 2018/12/04 | $(2.154 \pm 0.397) \times 10^{27}$ | $102.235 \pm 4.295$ | $17.566 \pm 2.211$ | L. Petrov (2018) |
| | | *X* | 2018/12/04 | $(1.605 \pm 0.227) \times 10^{27}$ | $104.758 \pm 4.193$ | $10.693 \pm 1.977$ | L. Petrov (2018) |
| J1035+5628 | 0.460 | *S* | 2017/01/31 | $(9.629 \pm 1.232) \times 10^{26}$ | $175.834 \pm 1.584$ | $12.251 \pm 1.001$ | L. Petrov (2018) |
| | | *X* | 2017/01/31 | $(3.597 \pm 0.443) \times 10^{26}$ | $184.907 \pm 0.824$ | $3.362 \pm 0.247$ | L. Petrov (2018) |
| J1111+1955 | 0.299 | *S* | 2018/03/26 | $(2.797 \pm 0.504) \times 10^{26}$ | $64.440 \pm 2.199$ | $10.796 \pm 1.546$ | L. Petrov (2018) |
| | | *X* | 2018/03/26 | $(7.652 \pm 1.359) \times 10^{25}$ | $74.660 \pm 0.726$ | $3.762 \pm 0.482$ | L. Petrov (2018) |
| J1120+1420 | 0.362 | *S* | 2018/04/08 | $(7.019 \pm 1.488) \times 10^{26}$ | $413.702 \pm 5.546$ | $22.207 \pm 3.777$ | L. Petrov (2018) |
| | | *X* | 2018/04/08 | $(5.887 \pm 1.587) \times 10^{25}$ | ... | $8.889 \pm 1.229$ | L. Petrov (2018) |
| J1227+3635 | 1.975 | *S* | 1996/06/07 | $(6.109 \pm 0.879) \times 10^{28}$ | $396.904 \pm 20.518$ | $25.849 \pm 5.197$ | A. Beasley et al. (2002) |
| | | *X* | 1996/06/07 | $(1.071 \pm 0.290) \times 10^{28}$ | ... | $10.443 \pm 0.868$ | A. Beasley et al. (2002) |
| J1247+6723 | 0.107219 | *S* | 2018/07/01 | $(6.853 \pm 0.825) \times 10^{24}$ | $14.626 \pm 0.116$ | $1.051 \pm 0.075$ | L. Petrov (2018) |
| | | *X* | 2018/07/01 | $(3.293 \pm 0.466) \times 10^{24}$ | $16.106 \pm 0.136$ | $1.050 \pm 0.088$ | L. Petrov (2018) |
| J1511+0518 | 0.084 | *S* | 2002/01/31 | $(2.932 \pm 0.438) \times 10^{24}$ | $7.119 \pm 0.522$ | $2.242 \pm 0.324$ | E. Fomalont et al. (2003) |
| | | *X* | 2002/01/31 | $(9.637 \pm 1.155) \times 10^{24}$ | $7.411 \pm 0.125$ | $0.844 \pm 0.079$ | E. Fomalont et al. (2003) |
| J1734+0926 | 0.735 | *S* | 1995/07/15 | $(2.936 \pm 0.244) \times 10^{27}$ | $87.144 \pm 1.020$ | $8.978 \pm 0.572$ | A. Beasley et al. (2002) |
| | | *X* | 1995/07/15 | $(1.011 \pm 0.163) \times 10^{27}$ | $97.668 \pm 0.839$ | $3.038 \pm 0.337$ | A. Beasley et al. (2002) |
| J1735+5049 | 0.835 | *S* | 1996/08/10 | $(1.250 \pm 0.114) \times 10^{27}$ | $15.634 \pm 0.688$ | $8.741 \pm 0.466$ | A. Beasley et al. (2002) |
| | | *C* | 1996/08/22 | $(1.442 \pm 0.186) \times 10^{27}$ | $20.633 \pm 0.629$ | $5.880 \pm 0.407$ | J. Helmboldt et al. (2007) |
| | | *X* | 1996/08/10 | $(1.384 \pm 0.191) \times 10^{27}$ | $24.910 \pm 0.651$ | $3.355 \pm 0.359$ | A. Beasley et al. (2002) |
| J1944+5448 | 0.263 | *S* | 1994/08/12 | $(3.066 \pm 0.423) \times 10^{26}$ | $153.281 \pm 0.695$ | $4.785 \pm 0.363$ | A. Beasley et al. (2002) |
| | | *X* | 1994/08/12 | $(8.675 \pm 1.781) \times 10^{25}$ | $156.113 \pm 0.901$ | $3.211 \pm 0.525$ | A. Beasley et al. (2002) |
| J2203+1007 | 1.005 | *S* | 2018/01/25 | $(6.638 \pm 0.702) \times 10^{26}$ | $70.624 \pm 2.232$ | $17.364 \pm 1.402$ | L. Petrov (2018) |
| | | *X* | 2018/01/25 | $(5.548 \pm 0.645) \times 10^{26}$ | $79.006 \pm 1.213$ | $6.257 \pm 0.507$ | L. Petrov (2018) |

**Note.** J2000 ID: source name in J2000 coordinates; $z$: redshift; band: observational band (*S* or *X*); Obs Date: date of observation; Luminosity (W Hz$^{-1}$): luminosity at the given frequency in units of W Hz$^{-1}$; Linear Size (pc): linear size in parsecs; $r_{hs}$ (pc): hot spot radius in parsecs; References: reference to the source of the data. The intrinsic physical quantities of CSOs are derived based on the Pantheon+ SNe Ia sample (with the validity of CDDR).

**Table 2**
Best Fits to the Hot Spot Dynamical Model with Different CSO2.0 Samples

| Data | $s_L$ | $\sigma_{s_L}$ | $s_r$ | $\sigma_{s_r}$ | $s_{Lr}$ | $\sigma_{s_{Lr}}$ |
|---|---|---|---|---|---|---|
| Sample I | 1.376 | 0.467 | 0.433 | 0.186 | 2.443 | 0.438 |
| Sample II | 1.625 | 0.544 | 0.689 | 0.155 | 2.393 | 0.527 |
| Simulated sample | 1.533 | 0.017 | 1.040 | 0.002 | 1.482 | 0.013 |

semianalytical model of CSOs (A. G. Sullivan et al. 2024) and generate a simulated sample. To reduce sample dispersion and capture the overall trend of the *P–D* relation, we select a smaller jet energy range of $\{4M_{\odot}c^2, 6M_{\odot}c^2\}$. Additionally, the peak external medium density, $\rho_0$, is fixed at $10^{-23}$ g cm$^{-3}$. The jet open angle is fixed at 15°. The age of CSOs is limited by the period before the decline in jet power. All other parameters are consistent with those obtained in A. G. Sullivan et al. (2024). Finally, we simulate a sample of 200 early-stage CSO2.0s, and the results are shown in Table 4. More importantly, the *P–D* relation of CSOs highlights their significant potential in cosmology. While current observational constraints are limited by sample size, the advent of next-generation VLBI surveys promises to substantially expand the CSO population. We will demonstrate the potential of this approach, using carefully constructed simulated samples based on our current understanding of CSO physics.

The semianalytical model developed by A. G. Sullivan et al. (2024) does not rely on a specific cosmological model; however, it is instead based on the minimum energy assumption and the unmagnetized, gas-pressure-collimated jet model (O. Bromberg et al. 2011; W. A. Baan & T. An 2025). Notably, by extending the classical de Laval nozzle theory to account for ambient pressure gradients, W. A. Baan & T. An (2025) illustrated how ambient pressure gradients drive jet acceleration and collimation across different astrophysical scales. Since the semianalytical model provides

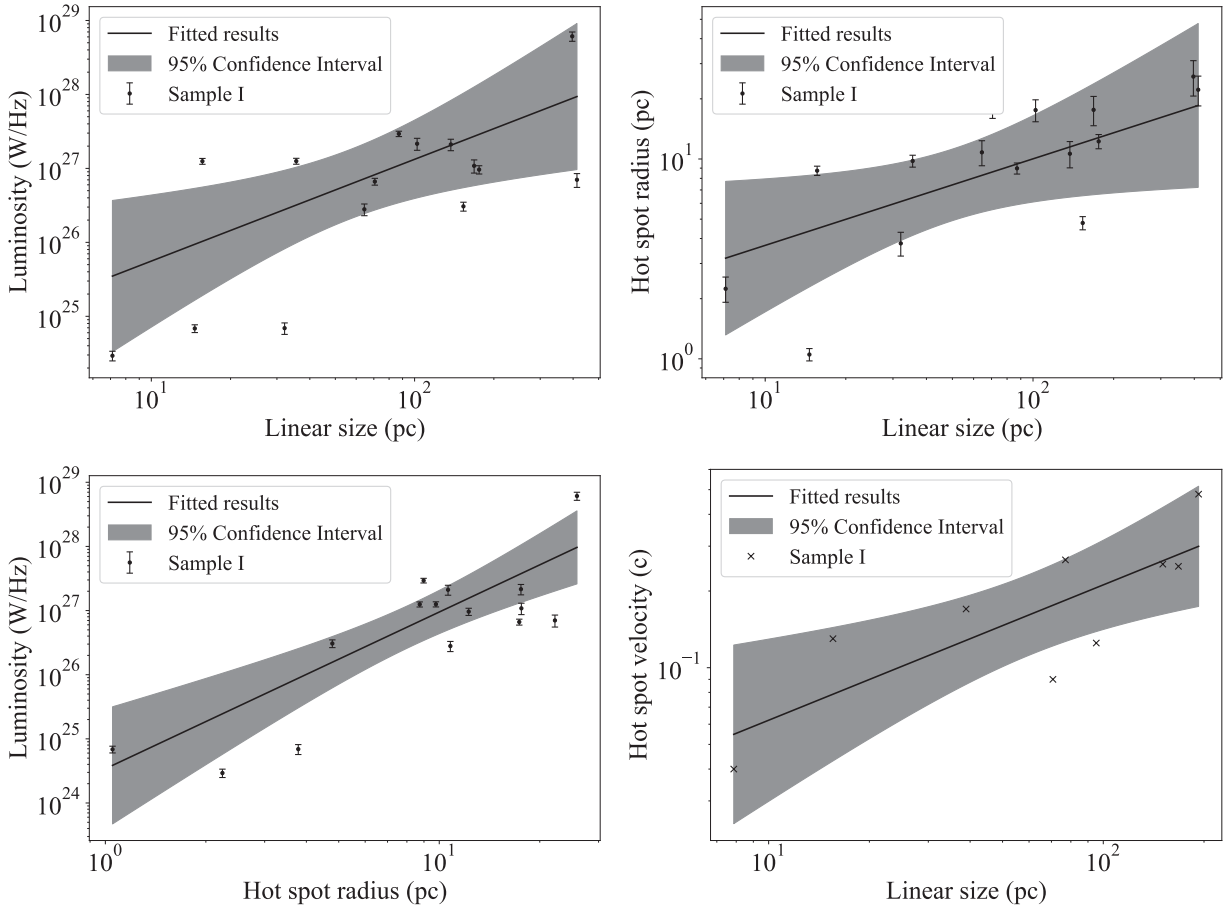


**Figure 2.** Fits to CSO2.0 sample calibrated by the Pantheon+SH0ES SNe Ia (D. Brout et al. 2022; A. G. Riess et al. 2022) (with the validity of CDDR). (a) The best-fit results for the linear size and the luminosity. (b) The best-fit results for the linear size and the hot spot radius. (c) The best-fit results for the hot spot radius and the luminosity. (d) The best-fit results for the hot spot velocity and linear size.

the intrinsic physical parameters, including the luminosity and linear size, it should be carefully translated into observable quantities to realistically simulate observational data.

Therefore, to mimic the current observation, analyzing the distribution of the available sample is essential. A strong correlation is found between the luminosity and the redshift in the current sample, where high-luminosity CSOs are more likely to appear at higher redshift. We interpret this correlation as arising from the sensitivity limits of current VLBI observations. Kernel density estimation (KDE) is a nonparametric technique used to estimate the probability density function of a random variable from a finite data sample with increased accuracy, and it was proposed by E. Parzen (1962), R. A. Davis et al. (2011). We perform a two-dimensional KDE on the luminosity and redshift data from the current sample, as illustrated in Figure 5. Using these results, one could assign redshifts to the simulated CSOs. Now we combine the distance information reconstructed from the Pantheon+SH0ES SNe Ia sample (D. Brout et al. 2022; A. G. Riess et al. 2022) and the galaxy cluster sample (E. De Filippis et al. 2005) in Section 3, to estimate the flux density and angular size for each simulated CSO. The distributions of the observables are shown in Figure 6. It can be seen that the redshift distribution of the simulated sample is more concentrated in the lower redshift range. We attribute this phenomenon primarily to the use of a smaller range of black hole mass, which is the key factor determining the energy of the jet and the range of peak luminosities (A. G. Sullivan et al. 2024).

After assigning the observational quantities to the simulated CSO sample, we implement a rigorous error analysis framework. Similarly, to mimic the current observation, we undertake a statistical analysis of the errors in the available sample. In cases of similar sensitivity and resolution, smaller observational quantities are expected to have larger relative errors. For the current CSO2.0 sample, a negative correlation is determined between angular separation size and its fractional uncertainty, suggesting the domination of resolution effects over sensitivity limits for size determination. The results are presented in the upper panel of Figure 7. However, weak evidence of such a negative correlation is found between flux density and its fractional uncertainty in the current sample, and the relative error is significantly large due to the high rms error in the residual map. Such a conclusion could be attributed to the fact that only a few circular Gaussian components are used to extract the brightness distribution from the UV data, which may result in some faint components being inadequately modeled. Therefore, we perform a Kolmogorov–Smirnov test for Gaussianity, with the $p$-value of $p = 0.661$, indicating that the relative error of flux density approximately follows a normal distribution. A similar method is applied to analyze the relative errors of the hot spot radius with the $p$-value of $p = 0.319$. The quantile–quantile plots are displayed in the middle and bottom panels of Figure 7, presenting the

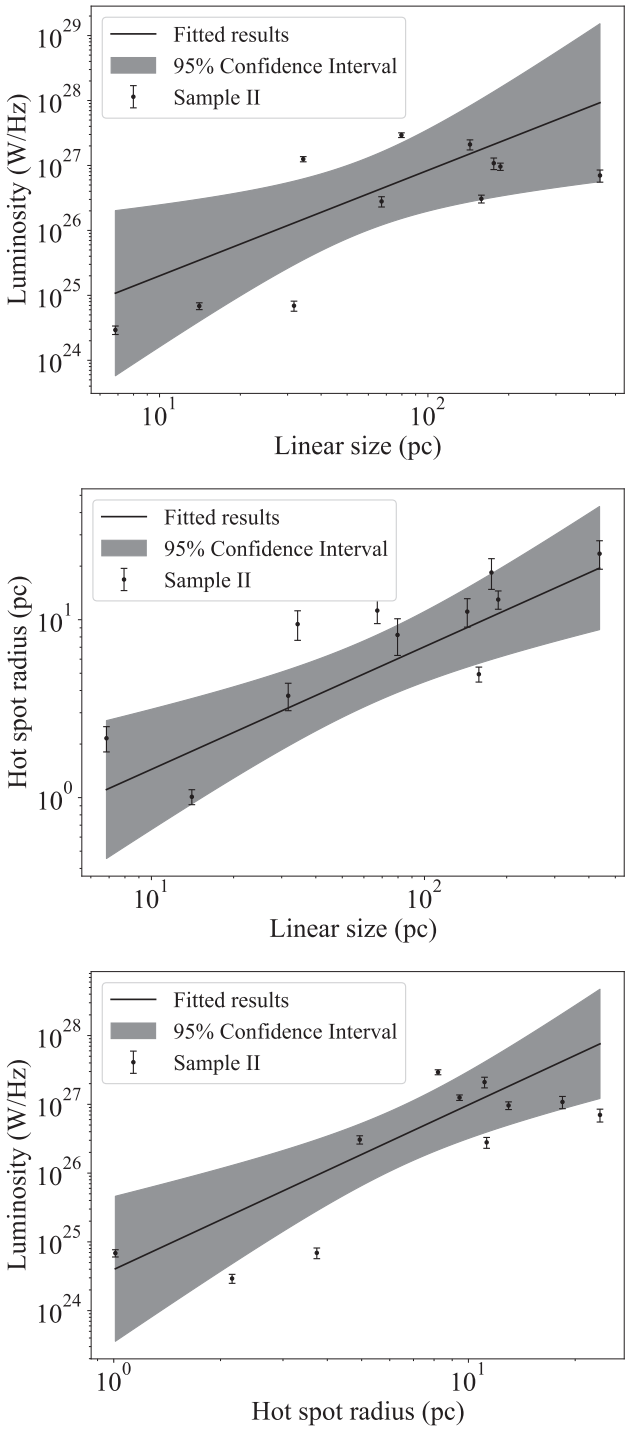


**Figure 3.** Fits to low-redshift CSO2.0 sample calibrated by the Pantheon +SH0ES SNe Ia (D. Brout et al. 2022; A. G. Riess et al. 2022) and galaxy cluster sample (E. De Filippis et al. 2005). (a) The best-fit results for the linear size and the luminosity. (b) The best-fit results for the linear size and the hot spot radius. (c) The best-fit results for the hot spot radius and the luminosity. (d) The best-fit results for the hot spot velocity and linear size.

Gaussianity test for the fractional uncertainties of flux density and angular separation size. Based on the Gaussian distributions shown in Figure 7, one could assign random observational uncertainties to different observables in the simulated CSO sample.

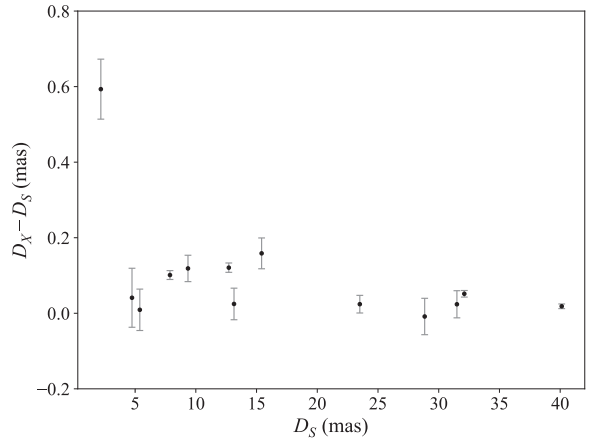


**Figure 4.** Differences in the distances between two hot spots in the *S* and *X* bands.

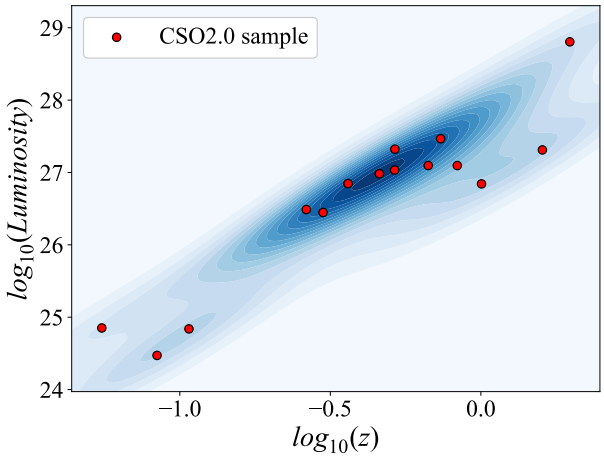


**Figure 5.** 2D KDE of redshift and luminosity for CSO2.0 sample.

**Table 3**
Differences in the Linear Size between Different Bands

| $(D_C - D_S)/D_S$ | $(D_X - D_S)/D_S$ | $(D_U - D_S)/D_S$ |
|---|---|---|
| 0.0673 ± 0.1420 | 0.0982 ± 0.1574 | 0.0507 ± 0.0005 |

Based on the above procedure, we successfully assigned observables to the simulated sample, with observational uncertainties at the same level as the current observations. The intrinsic physical quantities of simulated CSOs, with the uncertainties calculated from the corresponding observables, are summarized in Table 4. The least squares method is applied to fit the relations between luminosity, hot spot radius, and the linear size, with the results presented in Table 2. For the simulated sample, the three parameters characterizing the hot spot dynamical model are determined as $\beta = 1.132 \pm 0.007$, $\epsilon = 1.364 \pm 0.017$, and $\delta = 0.988 \pm 0.011$. As is shown in Figure 8, the relation between luminosity and linear size is similar for the currently available and simulated data. However, the hot spot radius may appear larger if the hot spot wiggles, as seen in Cygnus A (A. G. Sullivan et al. 2024). Therefore, this model only provides a lower limit for the hot spot radius. This is well supported by the fitting results, where the intercepts in both the hot spot radius–luminosity and hot spot radius–linear size relations are significantly smaller than those of the current sample, indicating that the model generally

**Table 4**
Simulated CSO2.0 Sample Based on the Semianalytical CSO Model (A. G. Sullivan et al. 2024)

| $z$ | Linear Size (pc) | Luminosity (W Hz$^{-1}$) | $v$ ($c$) | $r_{hs}$ (pc) | $z$ | Linear Size (pc) | Luminosity (W Hz$^{-1}$) | $v$ ($c$) | $r_{hs}$ (pc) |
|---|---|---|---|---|---|---|---|---|---|
| 0.010 | 0.770 ± 0.032 | (3.101 ± 0.364) × $10^{22}$ | 0.122 | 0.012 ± 0.001 | 0.251 | 183.075 ± 3.144 | (2.343 ± 0.320) × $10^{26}$ | 0.222 | 3.761 ± 0.491 |
| 0.018 | 2.357 ± 0.074 | (2.433 ± 0.331) × $10^{23}$ | 0.148 | 0.040 ± 0.004 | 0.253 | 220.522 ± 4.669 | (2.098 ± 0.373) × $10^{26}$ | 0.201 | 4.312 ± 0.553 |
| 0.032 | 6.669 ± 0.165 | (1.366 ± 0.224) × $10^{24}$ | 0.167 | 0.119 ± 0.017 | 0.253 | 241.546 ± 3.025 | (2.150 ± 0.317) × $10^{26}$ | 0.196 | 4.664 ± 0.400 |
| 0.037 | 1.577 ± 0.072 | (1.034 ± 0.167) × $10^{23}$ | 0.134 | 0.026 ± 0.004 | 0.255 | 139.197 ± 1.993 | (1.529 ± 0.194) × $10^{26}$ | 0.217 | 2.826 ± 0.437 |
| 0.037 | 4.862 ± 0.167 | (1.033 ± 0.173) × $10^{24}$ | 0.172 | 0.089 ± 0.008 | 0.255 | 109.000 ± 1.637 | (6.793 ± 0.899) × $10^{25}$ | 0.188 | 2.058 ± 0.228 |
| 0.040 | 4.063 ± 0.156 | (4.916 ± 0.616) × $10^{23}$ | 0.149 | 0.069 ± 0.006 | 0.256 | 233.983 ± 4.718 | (3.705 ± 0.405) × $10^{26}$ | 0.232 | 4.911 ± 0.635 |
| 0.048 | 11.892 ± 0.257 | (4.827 ± 0.510) × $10^{24}$ | 0.195 | 0.230 ± 0.034 | 0.256 | 88.226 ± 1.506 | (5.047 ± 0.874) × $10^{25}$ | 0.186 | 1.659 ± 0.209 |
| 0.049 | 15.109 ± 0.261 | (3.039 ± 0.490) × $10^{24}$ | 0.157 | 0.261 ± 0.033 | 0.259 | 54.420 ± 1.039 | (2.854 ± 0.453) × $10^{25}$ | 0.188 | 1.028 ± 0.150 |
| 0.054 | 10.321 ± 0.216 | (3.701 ± 0.562) × $10^{24}$ | 0.190 | 0.197 ± 0.031 | 0.261 | 235.193 ± 4.370 | (3.195 ± 0.371) × $10^{26}$ | 0.222 | 4.828 ± 0.594 |
| 0.054 | 23.703 ± 0.420 | (7.092 ± 0.953) × $10^{24}$ | 0.170 | 0.426 ± 0.032 | 0.261 | 203.527 ± 3.546 | (2.457 ± 0.281) × $10^{26}$ | 0.217 | 4.131 ± 0.434 |
| 0.055 | 15.562 ± 0.412 | (3.553 ± 0.551) × $10^{24}$ | 0.162 | 0.274 ± 0.040 | 0.261 | 243.067 ± 3.703 | (2.156 ± 0.310) × $10^{26}$ | 0.196 | 4.689 ± 0.456 |
| 0.057 | 18.505 ± 0.349 | (7.984 ± 1.059) × $10^{24}$ | 0.192 | 0.354 ± 0.050 | 0.262 | 227.138 ± 4.010 | (2.366 ± 0.340) × $10^{26}$ | 0.206 | 4.495 ± 0.505 |
| 0.070 | 6.317 ± 0.223 | (1.113 ± 0.146) × $10^{24}$ | 0.160 | 0.111 ± 0.012 | 0.262 | 224.637 ± 3.721 | (3.204 ± 0.448) × $10^{26}$ | 0.226 | 4.652 ± 0.715 |
| 0.074 | 48.975 ± 0.934 | (2.292 ± 0.364) × $10^{25}$ | 0.183 | 0.914 ± 0.075 | 0.267 | 168.412 ± 3.011 | (2.005 ± 0.320) × $10^{26}$ | 0.219 | 3.434 ± 0.319 |
| 0.081 | 40.272 ± 0.662 | (1.708 ± 0.312) × $10^{25}$ | 0.181 | 0.746 ± 0.064 | 0.272 | 299.437 ± 5.656 | (3.118 ± 0.507) × $10^{26}$ | 0.202 | 5.868 ± 0.936 |
| 0.085 | 30.426 ± 0.572 | (1.315 ± 0.189) × $10^{25}$ | 0.185 | 0.571 ± 0.064 | 0.276 | 258.927 ± 4.493 | (5.223 ± 0.737) × $10^{26}$ | 0.247 | 5.605 ± 0.678 |
| 0.086 | 80.475 ± 1.026 | (5.801 ± 0.998) × $10^{25}$ | 0.200 | 1.568 ± 0.233 | 0.276 | 203.283 ± 2.570 | (2.288 ± 0.381) × $10^{26}$ | 0.213 | 4.084 ± 0.609 |
| 0.088 | 52.059 ± 1.004 | (2.260 ± 0.360) × $10^{25}$ | 0.179 | 0.959 ± 0.091 | 0.283 | 70.321 ± 1.726 | (6.628 ± 1.057) × $10^{25}$ | 0.218 | 1.432 ± 0.196 |
| 0.089 | 38.314 ± 0.941 | (1.252 ± 0.182) × $10^{25}$ | 0.168 | 0.685 ± 0.084 | 0.289 | 147.638 ± 3.080 | (2.227 ± 0.407) × $10^{26}$ | 0.237 | 3.129 ± 0.368 |
| 0.089 | 22.815 ± 0.552 | (6.390 ± 0.941) × $10^{24}$ | 0.167 | 0.407 ± 0.034 | 0.291 | 191.855 ± 3.017 | (1.973 ± 0.239) × $10^{26}$ | 0.208 | 3.813 ± 0.572 |
| 0.092 | 39.544 ± 0.968 | (1.492 ± 0.215) × $10^{25}$ | 0.175 | 0.722 ± 0.076 | 0.297 | 126.430 ± 2.309 | (1.458 ± 0.207) × $10^{26}$ | 0.222 | 2.593 ± 0.413 |
| 0.097 | 6.935 ± 0.245 | (9.924 ± 1.643) × $10^{23}$ | 0.150 | 0.118 ± 0.014 | 0.297 | 249.956 ± 4.871 | (2.155 ± 0.397) × $10^{26}$ | 0.194 | 4.799 ± 0.636 |
| 0.105 | 50.052 ± 0.942 | (4.505 ± 0.832) × $10^{25}$ | 0.220 | 1.025 ± 0.123 | 0.298 | 203.096 ± 2.693 | (3.052 ± 0.393) × $10^{26}$ | 0.231 | 4.253 ± 0.420 |
| 0.108 | 57.830 ± 0.871 | (4.679 ± 0.602) × $10^{25}$ | 0.212 | 1.160 ± 0.140 | 0.302 | 250.856 ± 5.003 | (2.390 ± 0.332) × $10^{26}$ | 0.200 | 4.885 ± 0.586 |
| 0.112 | 14.238 ± 0.428 | (2.491 ± 0.304) × $10^{24}$ | 0.151 | 0.242 ± 0.023 | 0.307 | 144.467 ± 3.072 | (1.953 ± 0.271) × $10^{26}$ | 0.230 | 3.016 ± 0.222 |
| 0.116 | 67.643 ± 1.125 | (3.822 ± 0.591) × $10^{25}$ | 0.189 | 1.282 ± 0.114 | 0.309 | 184.818 ± 4.254 | (1.851 ± 0.239) × $10^{26}$ | 0.207 | 3.664 ± 0.438 |
| 0.120 | 29.137 ± 0.636 | (9.419 ± 1.173) × $10^{24}$ | 0.171 | 0.525 ± 0.072 | 0.309 | 268.145 ± 5.051 | (2.688 ± 0.303) × $10^{26}$ | 0.202 | 5.246 ± 0.825 |
| 0.127 | 128.072 ± 2.865 | (7.716 ± 1.261) × $10^{25}$ | 0.184 | 2.393 ± 0.239 | 0.309 | 186.638 ± 3.210 | (1.649 ± 0.268) × $10^{26}$ | 0.200 | 3.634 ± 0.526 |
| 0.130 | 79.588 ± 1.280 | (5.180 ± 0.850) × $10^{25}$ | 0.194 | 1.530 ± 0.156 | 0.312 | 164.037 ± 2.803 | (1.427 ± 0.232) × $10^{26}$ | 0.201 | 3.201 ± 0.297 |
| 0.137 | 56.045 ± 1.056 | (3.153 ± 0.400) × $10^{25}$ | 0.191 | 1.069 ± 0.084 | 0.316 | 252.404 ± 4.011 | (4.914 ± 0.664) × $10^{26}$ | 0.245 | 5.442 ± 0.609 |
| 0.138 | 169.464 ± 2.558 | (1.181 ± 0.151) × $10^{26}$ | 0.188 | 3.200 ± 0.225 | 0.316 | 249.146 ± 3.384 | (2.415 ± 0.364) × $10^{26}$ | 0.201 | 4.865 ± 0.726 |
| 0.144 | 42.445 ± 0.688 | (2.946 ± 0.481) × $10^{25}$ | 0.207 | 0.842 ± 0.067 | 0.321 | 247.729 ± 5.343 | (3.914 ± 0.532) × $10^{26}$ | 0.231 | 5.187 ± 0.516 |
| 0.145 | 59.800 ± 1.057 | (2.897 ± 0.343) × $10^{25}$ | 0.182 | 1.113 ± 0.099 | 0.322 | 347.220 ± 5.837 | (6.024 ± 0.900) × $10^{26}$ | 0.232 | 7.279 ± 0.654 |
| 0.147 | 38.942 ± 0.843 | (2.349 ± 0.320) × $10^{25}$ | 0.200 | 0.760 ± 0.096 | 0.323 | 126.747 ± 2.231 | (1.089 ± 0.140) × $10^{26}$ | 0.204 | 2.492 ± 0.353 |
| 0.148 | 51.584 ± 1.253 | (2.615 ± 0.318) × $10^{25}$ | 0.187 | 0.972 ± 0.135 | 0.324 | 166.707 ± 3.754 | (2.658 ± 0.440) × $10^{26}$ | 0.238 | 3.546 ± 0.280 |
| 0.148 | 128.794 ± 2.276 | (1.220 ± 0.138) × $10^{26}$ | 0.209 | 2.567 ± 0.293 | 0.332 | 271.633 ± 5.173 | (4.264 ± 0.728) × $10^{26}$ | 0.229 | 5.664 ± 0.870 |
| 0.151 | 13.621 ± 0.520 | (4.259 ± 0.535) × $10^{24}$ | 0.179 | 0.252 ± 0.034 | 0.340 | 95.188 ± 2.334 | (7.107 ± 0.822) × $10^{25}$ | 0.200 | 1.854 ± 0.148 |
| 0.152 | 143.944 ± 3.118 | (1.021 ± 0.174) × $10^{26}$ | 0.191 | 2.741 ± 0.220 | 0.342 | 276.036 ± 6.089 | (3.907 ± 0.687) × $10^{26}$ | 0.222 | 5.668 ± 0.746 |
| 0.152 | 128.366 ± 2.434 | (1.065 ± 0.151) × $10^{26}$ | 0.201 | 2.510 ± 0.273 | 0.342 | 74.246 ± 1.684 | (5.360 ± 0.691) × $10^{25}$ | 0.201 | 1.451 ± 0.127 |
| 0.152 | 99.503 ± 2.223 | (8.085 ± 1.063) × $10^{25}$ | 0.204 | 1.958 ± 0.272 | 0.347 | 335.694 ± 5.419 | (4.032 ± 0.648) × $10^{26}$ | 0.209 | 6.685 ± 0.905 |
| 0.152 | 115.000 ± 1.813 | (7.186 ± 1.089) × $10^{25}$ | 0.187 | 2.168 ± 0.222 | 0.350 | 111.140 ± 1.887 | (1.487 ± 0.229) × $10^{26}$ | 0.233 | 2.339 ± 0.323 |
| 0.153 | 81.070 ± 1.528 | (7.266 ± 1.173) × $10^{25}$ | 0.213 | 1.631 ± 0.153 | 0.357 | 236.614 ± 5.141 | (3.837 ± 0.659) × $10^{26}$ | 0.233 | 4.981 ± 0.440 |
| 0.154 | 109.937 ± 2.502 | (8.180 ± 1.058) × $10^{25}$ | 0.197 | 2.129 ± 0.193 | 0.360 | 98.217 ± 2.044 | (8.701 ± 0.965) × $10^{25}$ | 0.209 | 1.958 ± 0.247 |
| 0.155 | 65.506 ± 1.316 | (2.954 ± 0.430) × $10^{25}$ | 0.178 | 1.203 ± 0.153 | 0.369 | 84.760 ± 1.574 | (7.883 ± 1.432) × $10^{25}$ | 0.214 | 1.711 ± 0.207 |
| 0.155 | 290.357 ± 5.301 | (3.515 ± 0.505) × $10^{26}$ | 0.212 | 5.820 ± 0.866 | 0.370 | 184.577 ± 4.209 | (2.045 ± 0.249) × $10^{26}$ | 0.213 | 3.713 ± 0.322 |
| 0.157 | 168.445 ± 3.554 | (2.545 ± 0.292) × $10^{26}$ | 0.234 | 3.553 ± 0.520 | 0.375 | 94.012 ± 1.885 | (7.360 ± 0.876) × $10^{25}$ | 0.203 | 1.844 ± 0.214 |
| 0.157 | 185.462 ± 3.311 | (2.210 ± 0.343) × $10^{26}$ | 0.218 | 3.769 ± 0.323 | 0.378 | 133.424 ± 2.861 | (7.789 ± 0.855) × $10^{25}$ | 0.182 | 2.478 ± 0.316 |

**Table 4**
(Continued)

| $z$ | Linear Size (pc) | Luminosity (W Hz$^{-1}$) | $v$ ($c$) | $r_{hs}$ (pc) | $z$ | Linear Size (pc) | Luminosity (W Hz$^{-1}$) | $v$ ($c$) | $r_{hs}$ (pc) |
|---|---|---|---|---|---|---|---|---|---|
| 0.158 | 26.993 ± 0.639 | (9.360 ± 1.555) × $10^{24}$ | 0.175 | 0.494 ± 0.062 | 0.380 | 87.286 ± 1.804 | (6.552 ± 0.917) × $10^{25}$ | 0.201 | 1.707 ± 0.229 |
| 0.158 | 12.734 ± 0.320 | (4.518 ± 0.493) × $10^{24}$ | 0.186 | 0.240 ± 0.023 | 0.384 | 247.575 ± 5.413 | (3.293 ± 0.589) × $10^{26}$ | 0.220 | 5.059 ± 0.632 |
| 0.160 | 99.499 ± 1.303 | (1.067 ± 0.126) × $10^{26}$ | 0.221 | 2.038 ± 0.312 | 0.389 | 111.679 ± 2.317 | (1.225 ± 0.182) × $10^{26}$ | 0.220 | 2.285 ± 0.204 |
| 0.163 | 47.519 ± 0.754 | (3.469 ± 0.373) × $10^{25}$ | 0.208 | 0.946 ± 0.111 | 0.394 | 134.554 ± 2.196 | (1.268 ± 0.151) × $10^{26}$ | 0.208 | 2.675 ± 0.285 |
| 0.166 | 115.113 ± 1.749 | (9.553 ± 1.287) × $10^{25}$ | 0.203 | 2.260 ± 0.211 | 0.399 | 276.434 ± 5.157 | (3.025 ± 0.332) × $10^{26}$ | 0.206 | 5.471 ± 0.862 |
| 0.171 | 78.506 ± 1.537 | (7.321 ± 1.326) × $10^{25}$ | 0.216 | 1.590 ± 0.170 | 0.403 | 198.120 ± 3.517 | (2.582 ± 0.359) × $10^{26}$ | 0.222 | 4.069 ± 0.520 |
| 0.171 | 138.046 ± 3.093 | (9.556 ± 1.648) × $10^{25}$ | 0.190 | 2.624 ± 0.368 | 0.413 | 84.637 ± 1.984 | (7.362 ± 0.955) × $10^{25}$ | 0.210 | 1.692 ± 0.199 |
| 0.174 | 27.941 ± 0.562 | (1.207 ± 0.200) × $10^{25}$ | 0.186 | 0.527 ± 0.067 | 0.415 | 228.140 ± 4.984 | (3.739 ± 0.515) × $10^{26}$ | 0.235 | 4.817 ± 0.613 |
| 0.174 | 73.900 ± 1.320 | (6.150 ± 0.806) × $10^{25}$ | 0.210 | 1.476 ± 0.126 | 0.416 | 111.918 ± 2.372 | (1.280 ± 0.237) × $10^{26}$ | 0.223 | 2.303 ± 0.281 |
| 0.174 | 131.697 ± 2.169 | (1.110 ± 0.187) × $10^{26}$ | 0.202 | 2.579 ± 0.398 | 0.416 | 143.909 ± 2.504 | (1.423 ± 0.245) × $10^{26}$ | 0.210 | 2.874 ± 0.239 |
| 0.174 | 63.696 ± 1.449 | (3.595 ± 0.521) × $10^{25}$ | 0.190 | 1.209 ± 0.176 | 0.416 | 269.394 ± 4.472 | (4.361 ± 0.722) × $10^{26}$ | 0.231 | 5.644 ± 0.580 |
| 0.176 | 54.062 ± 0.950 | (2.033 ± 0.338) × $10^{25}$ | 0.171 | 0.974 ± 0.079 | 0.417 | 155.530 ± 3.389 | (1.408 ± 0.248) × $10^{26}$ | 0.204 | 3.058 ± 0.316 |
| 0.177 | 149.104 ± 2.866 | (9.569 ± 1.335) × $10^{25}$ | 0.185 | 2.796 ± 0.337 | 0.420 | 158.274 ± 2.582 | (1.965 ± 0.361) × $10^{26}$ | 0.223 | 3.254 ± 0.407 |
| 0.179 | 162.745 ± 2.229 | (1.393 ± 0.197) × $10^{26}$ | 0.200 | 3.170 ± 0.226 | 0.424 | 79.312 ± 1.547 | (5.112 ± 0.869) × $10^{25}$ | 0.194 | 1.523 ± 0.211 |
| 0.182 | 77.065 ± 1.207 | (6.926 ± 1.077) × $10^{25}$ | 0.214 | 1.553 ± 0.227 | 0.434 | 329.280 ± 5.499 | (3.881 ± 0.470) × $10^{26}$ | 0.208 | 6.544 ± 1.033 |
| 0.186 | 126.153 ± 2.526 | (1.207 ± 0.223) × $10^{26}$ | 0.210 | 2.519 ± 0.271 | 0.443 | 52.527 ± 1.383 | (2.434 ± 0.325) × $10^{25}$ | 0.182 | 0.976 ± 0.151 |
| 0.186 | 149.608 ± 1.937 | (1.474 ± 0.173) × $10^{26}$ | 0.209 | 2.982 ± 0.359 | 0.445 | 295.261 ± 3.709 | (5.632 ± 0.928) × $10^{26}$ | 0.241 | 6.311 ± 0.815 |
| 0.186 | 105.481 ± 2.099 | (7.297 ± 0.977) × $10^{25}$ | 0.194 | 2.024 ± 0.289 | 0.453 | 298.717 ± 5.608 | (3.111 ± 0.538) × $10^{26}$ | 0.202 | 5.853 ± 0.793 |
| 0.192 | 146.166 ± 3.219 | (1.691 ± 0.282) × $10^{26}$ | 0.219 | 2.984 ± 0.282 | 0.457 | 150.436 ± 2.810 | (1.755 ± 0.252) × $10^{26}$ | 0.219 | 3.072 ± 0.389 |
| 0.197 | 86.641 ± 1.486 | (7.479 ± 0.874) × $10^{25}$ | 0.209 | 1.729 ± 0.152 | 0.457 | 170.562 ± 2.628 | (1.333 ± 0.151) × $10^{26}$ | 0.194 | 3.273 ± 0.437 |
| 0.197 | 230.330 ± 4.412 | (2.645 ± 0.389) × $10^{26}$ | 0.212 | 4.620 ± 0.553 | 0.458 | 342.299 ± 7.472 | (4.648 ± 0.694) × $10^{26}$ | 0.216 | 6.933 ± 1.045 |
| 0.199 | 59.048 ± 1.417 | (3.621 ± 0.609) × $10^{25}$ | 0.195 | 1.138 ± 0.169 | 0.465 | 165.409 ± 3.962 | (1.422 ± 0.229) × $10^{26}$ | 0.200 | 3.222 ± 0.482 |
| 0.199 | 169.548 ± 3.047 | (1.746 ± 0.275) × $10^{26}$ | 0.210 | 3.385 ± 0.402 | 0.467 | 272.140 ± 6.133 | (2.850 ± 0.433) × $10^{26}$ | 0.204 | 5.355 ± 0.661 |
| 0.199 | 53.434 ± 1.227 | (3.085 ± 0.521) × $10^{25}$ | 0.193 | 1.025 ± 0.121 | 0.467 | 284.467 ± 4.862 | (2.716 ± 0.382) × $10^{26}$ | 0.198 | 5.515 ± 0.787 |
| 0.203 | 179.024 ± 2.349 | (1.528 ± 0.248) × $10^{26}$ | 0.198 | 3.473 ± 0.496 | 0.473 | 260.471 ± 5.018 | (5.111 ± 0.587) × $10^{26}$ | 0.245 | 5.616 ± 0.436 |
| 0.204 | 227.872 ± 2.920 | (1.957 ± 0.358) × $10^{26}$ | 0.195 | 4.386 ± 0.445 | 0.503 | 291.960 ± 5.210 | (3.469 ± 0.464) × $10^{26}$ | 0.210 | 5.835 ± 0.466 |
| 0.207 | 133.793 ± 2.023 | (9.959 ± 1.130) × $10^{25}$ | 0.195 | 2.572 ± 0.223 | 0.504 | 256.850 ± 4.500 | (2.972 ± 0.444) × $10^{26}$ | 0.211 | 5.137 ± 0.733 |
| 0.208 | 220.089 ± 4.380 | (3.943 ± 0.510) × $10^{26}$ | 0.241 | 4.712 ± 0.598 | 0.507 | 274.921 ± 5.913 | (3.842 ± 0.712) × $10^{26}$ | 0.221 | 5.636 ± 0.595 |
| 0.209 | 82.398 ± 1.316 | (6.108 ± 1.109) × $10^{25}$ | 0.201 | 1.611 ± 0.247 | 0.515 | 219.952 ± 4.343 | (2.911 ± 0.344) × $10^{26}$ | 0.221 | 4.510 ± 0.361 |
| 0.210 | 280.279 ± 4.144 | (3.605 ± 0.595) × $10^{26}$ | 0.216 | 5.673 ± 0.566 | 0.517 | 302.751 ± 4.193 | (4.204 ± 0.534) × $10^{26}$ | 0.219 | 6.179 ± 0.602 |
| 0.215 | 137.095 ± 2.327 | (1.083 ± 0.156) × $10^{26}$ | 0.198 | 2.656 ± 0.304 | 0.562 | 286.486 ± 4.766 | (3.252 ± 0.529) × $10^{26}$ | 0.208 | 5.692 ± 0.748 |
| 0.217 | 71.276 ± 1.760 | (6.804 ± 0.946) × $10^{25}$ | 0.219 | 1.453 ± 0.155 | 0.566 | 243.364 ± 3.958 | (3.922 ± 0.711) × $10^{26}$ | 0.233 | 5.114 ± 0.790 |
| 0.217 | 126.463 ± 2.090 | (1.137 ± 0.160) × $10^{26}$ | 0.206 | 2.503 ± 0.329 | 0.568 | 263.689 ± 5.102 | (2.364 ± 0.251) × $10^{26}$ | 0.196 | 5.080 ± 0.603 |
| 0.222 | 106.376 ± 1.947 | (5.411 ± 0.720) × $10^{25}$ | 0.177 | 1.953 ± 0.235 | 0.572 | 317.052 ± 4.856 | (4.252 ± 0.685) × $10^{26}$ | 0.217 | 6.428 ± 0.512 |
| 0.223 | 151.260 ± 2.049 | (1.542 ± 0.259) × $10^{26}$ | 0.211 | 3.028 ± 0.307 | 0.584 | 126.201 ± 2.430 | (8.074 ± 1.294) × $10^{25}$ | 0.187 | 2.379 ± 0.343 |
| 0.226 | 128.304 ± 2.729 | (1.752 ± 0.316) × $10^{26}$ | 0.232 | 2.694 ± 0.201 | 0.584 | 108.287 ± 1.965 | (9.528 ± 1.198) × $10^{25}$ | 0.207 | 2.149 ± 0.239 |
| 0.226 | 164.438 ± 3.246 | (2.501 ± 0.426) × $10^{26}$ | 0.235 | 3.476 ± 0.310 | 0.593 | 195.857 ± 3.436 | (2.441 ± 0.441) × $10^{26}$ | 0.220 | 3.998 ± 0.450 |
| 0.228 | 157.812 ± 2.827 | (1.321 ± 0.186) × $10^{26}$ | 0.199 | 3.067 ± 0.364 | 0.598 | 208.903 ± 3.516 | (3.229 ± 0.576) × $10^{26}$ | 0.232 | 4.387 ± 0.503 |
| 0.229 | 198.970 ± 2.961 | (2.070 ± 0.272) × $10^{26}$ | 0.208 | 3.955 ± 0.409 | 0.650 | 267.110 ± 4.176 | (3.218 ± 0.575) × $10^{26}$ | 0.213 | 5.367 ± 0.406 |
| 0.231 | 109.910 ± 2.541 | (1.415 ± 0.184) × $10^{26}$ | 0.231 | 2.302 ± 0.344 | 0.659 | 225.874 ± 4.251 | (2.582 ± 0.276) × $10^{26}$ | 0.212 | 4.530 ± 0.325 |
| 0.232 | 158.126 ± 2.012 | (1.315 ± 0.243) × $10^{26}$ | 0.199 | 3.070 ± 0.268 | 0.672 | 204.179 ± 3.493 | (2.028 ± 0.253) × $10^{26}$ | 0.205 | 4.028 ± 0.450 |
| 0.234 | 94.059 ± 2.045 | (1.093 ± 0.133) × $10^{26}$ | 0.227 | 1.952 ± 0.303 | 0.680 | 198.456 ± 3.288 | (1.469 ± 0.206) × $10^{26}$ | 0.189 | 3.759 ± 0.495 |
| 0.237 | 204.780 ± 3.496 | (2.649 ± 0.295) × $10^{26}$ | 0.221 | 4.196 ± 0.541 | 0.688 | 213.005 ± 4.509 | (1.969 ± 0.219) × $10^{26}$ | 0.200 | 4.154 ± 0.594 |
| 0.238 | 215.676 ± 4.168 | (2.802 ± 0.334) × $10^{26}$ | 0.221 | 4.414 ± 0.446 | 0.692 | 269.953 ± 5.143 | (3.907 ± 0.604) × $10^{26}$ | 0.224 | 5.565 ± 0.753 |
| 0.238 | 160.107 ± 3.608 | (1.423 ± 0.177) × $10^{26}$ | 0.202 | 3.137 ± 0.288 | 0.695 | 274.839 ± 4.312 | (2.710 ± 0.420) × $10^{26}$ | 0.200 | 5.360 ± 0.604 |
| 0.239 | 87.546 ± 2.089 | (7.360 ± 0.899) × $10^{25}$ | 0.208 | 1.739 ± 0.209 | 0.702 | 128.748 ± 2.124 | (1.550 ± 0.196) × $10^{26}$ | 0.224 | 2.655 ± 0.404 |
| 0.241 | 78.499 ± 1.718 | (5.252 ± 0.613) × $10^{25}$ | 0.196 | 1.516 ± 0.148 | 0.747 | 108.504 ± 2.044 | (8.639 ± 1.010) × $10^{25}$ | 0.201 | 2.123 ± 0.247 |

**Table 4**
(Continued)

| $z$ | Linear Size (pc) | Luminosity (W Hz$^{-1}$) | $v$ ($c$) | $r_{hs}$ (pc) | $z$ | Linear Size (pc) | Luminosity (W Hz$^{-1}$) | $v$ ($c$) | $r_{hs}$ (pc) |
|---|---|---|---|---|---|---|---|---|---|
| 0.244 | 102.916 ± 1.695 | (8.149 ± 0.975) × $10^{25}$ | 0.202 | 2.015 ± 0.225 | 0.751 | 260.193 ± 4.460 | (5.012 ± 0.529) × $10^{26}$ | 0.244 | 5.596 ± 0.505 |
| 0.245 | 239.188 ± 3.633 | (3.136 ± 0.496) × $10^{26}$ | 0.220 | 4.883 ± 0.368 | 0.789 | 327.248 ± 6.991 | (3.694 ± 0.590) × $10^{26}$ | 0.206 | 6.466 ± 0.998 |
| 0.245 | 234.985 ± 3.415 | (1.988 ± 0.284) × $10^{26}$ | 0.194 | 4.509 ± 0.375 | 0.796 | 187.810 ± 4.418 | (2.882 ± 0.362) × $10^{26}$ | 0.234 | 3.956 ± 0.417 |
| 0.246 | 181.489 ± 4.083 | (1.946 ± 0.331) × $10^{26}$ | 0.211 | 3.636 ± 0.333 | 0.811 | 163.407 ± 2.868 | (1.992 ± 0.291) × $10^{26}$ | 0.221 | 3.347 ± 0.424 |
| 0.248 | 132.308 ± 2.080 | (8.835 ± 1.172) × $10^{25}$ | 0.189 | 2.505 ± 0.252 | 0.841 | 169.755 ± 2.499 | (2.323 ± 0.396) × $10^{26}$ | 0.228 | 3.530 ± 0.439 |
| 0.249 | 57.994 ± 1.239 | (4.734 ± 0.775) × $10^{25}$ | 0.212 | 1.164 ± 0.091 | 1.019 | 259.860 ± 4.085 | (5.468 ± 0.932) × $10^{26}$ | 0.250 | 5.658 ± 0.587 |

**Note.** $z$: redshift; LS: linear size in units of parsecs; luminosity: luminosity at the peak of the spectrum; $v$ ($c$): separation velocity in units of the speed of light; $r_{\rm hs}$: radius of hot spots in units of parsecs.

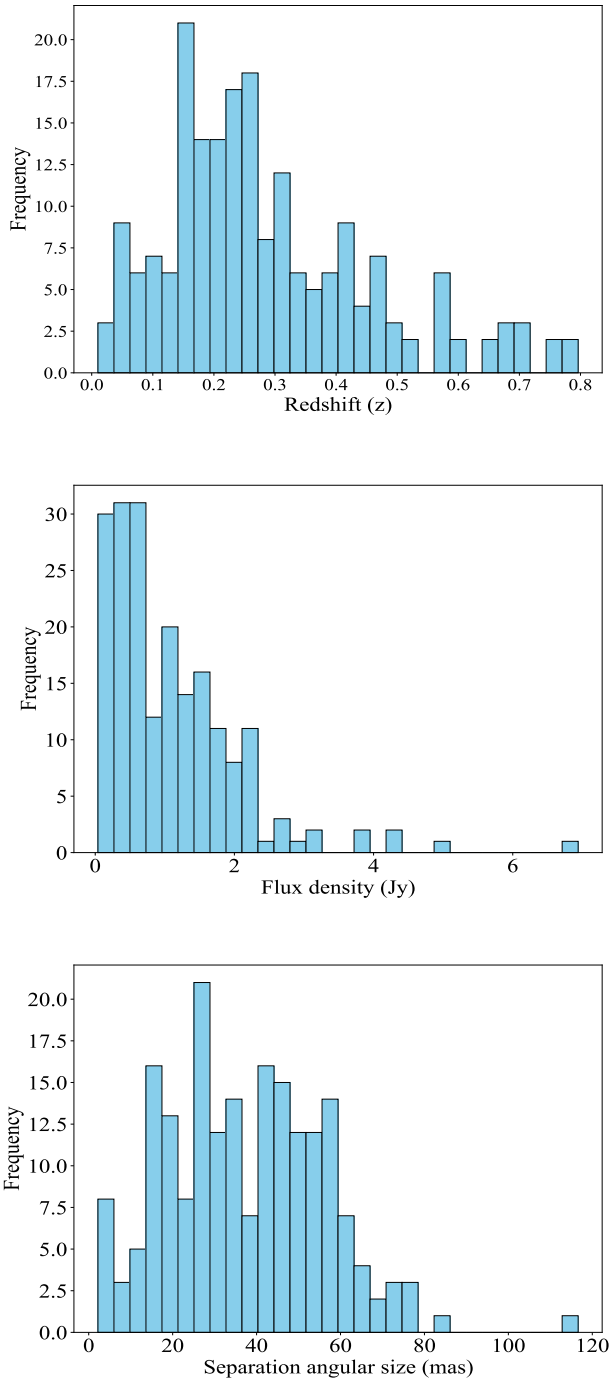


**Figure 6.** Upper panel: the redshift distribution of the simulated CSO2.0 sample. Middle panel: the flux density distribution of the simulated CSO2.0 sample. Lower panel: the angular separation size distribution of the simulated CSO2.0 sample.

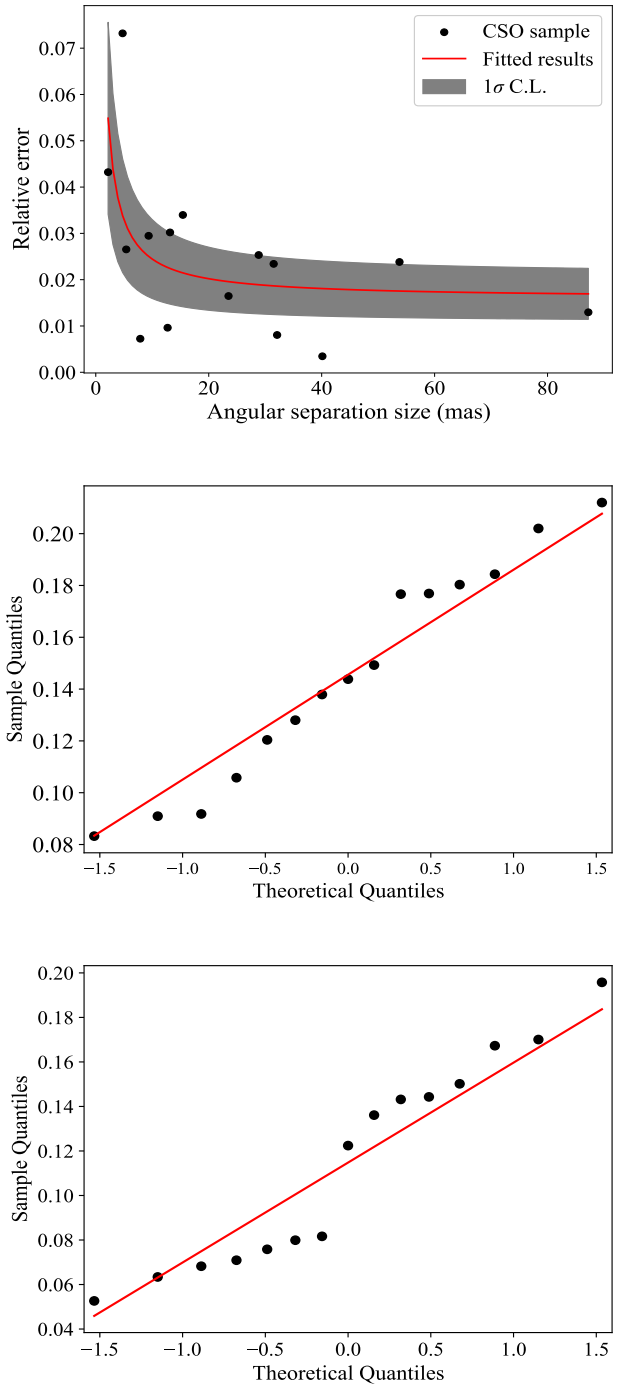


**Figure 7.** Upper panel: the relative error of the angular separation size. Middle panel: the quantile–quantile plot of the fractional uncertainty of the flux density. Lower panel: the quantile–quantile plot of the fractional uncertainty of the hot spot radius.

predicts a smaller hot spot radius compared to the current observations. The underestimation of the hot spot radius may lead to two critical issues: first, the angular size of the hot spot has approached or exceeded the limit resolution of the current VLBI observations; second, the wiggles on such small scales will strongly affect the robustness of the power-law relationship. Consequently, despite a more stringent power-law relation being found between the hot spot radius and luminosity, we do not apply it to the following cosmological applications.

For our simulated CSO sample, we calculate the luminosity of the sources using the reconstructed luminosity distance from the Pantheon+SH0ES SNe Ia sample. Using the observed angular separation $\theta$, we can determine the angular diameter distance through the angular size–redshift relation

$$D_A(z) = \frac{D}{\theta(z)}, \tag{7}$$

where $D$ is the linear size of CSO and $\theta(z)$ is the angular separation size at redshift $z$. The evolution of the angular

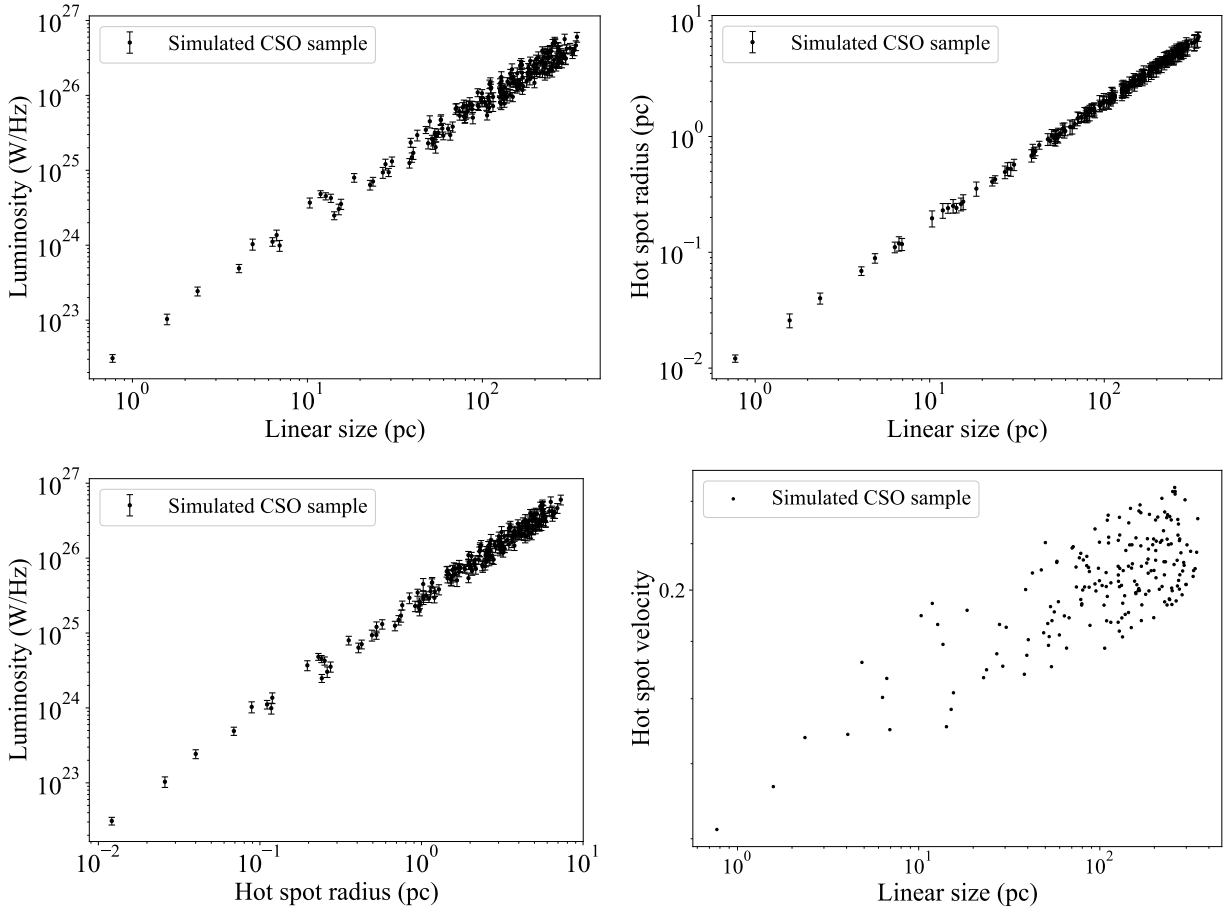


**Figure 8.** Fits to simulated CSO2.0 sample. (a) The relation between the linear size and the luminosity. (b) The relation between the linear size and the hot spot radius. (c) The relation between the hot spot radius and the luminosity. (d) The relation between the hot spot velocity and linear size.

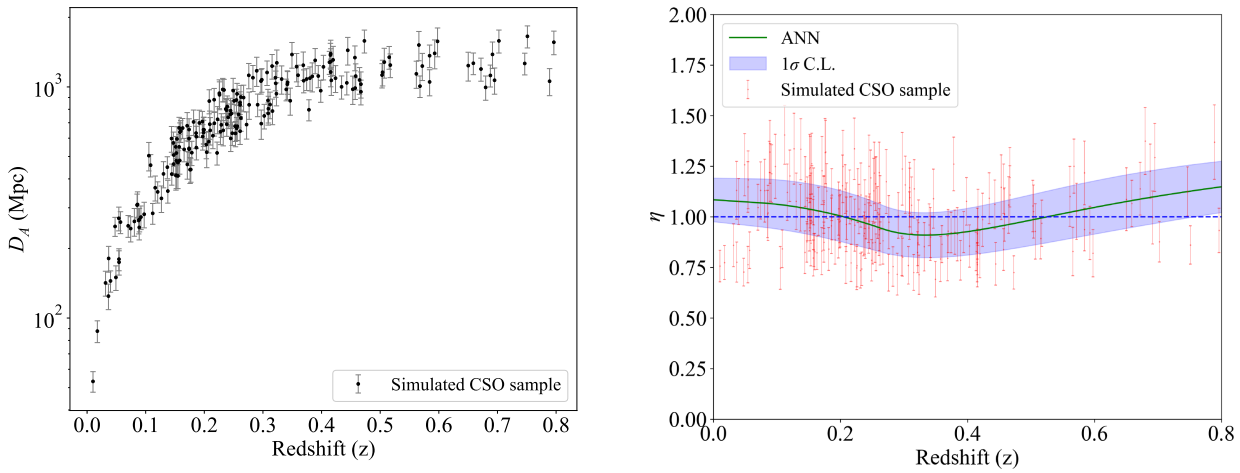


**Figure 9.** Angular diameter distances $D_A(z)$ (left panel) and CDDR parameter $\eta(z)$ (right panel) from the simulated CSO2.0 sample. The evolution of $\eta(z)$ with redshifts is also added, which is reconstructed with an ANN.

diameter distance with redshift is shown in Figure 9. Both the observational uncertainties and the fitting errors of the *P–D* relation are involved in the $D_A(z)$ measurements. It should be noted that, although a cosmologically model-independent semianalytical model is used in the CSO simulation, the *P–D* relation cannot provide independent angular diameter distance measurements. A straightforward cosmological application of the *P–D* relation is the well-known CDDR test. The CDDR represents a fundamental pillar of observational cosmology, emerging from two foundational principles: photon number conservation and light propagation along null geodesics in Riemannian spacetime. A violation of the first assumption is often used to constrain new physics (S. Cao & Z. Zhu 2011; S. Cao et al. 2016), while a violation of the second is employed

**Table 5**
Statistical Measurements of the CDDR Parameter Based on Different Statistical Approaches

| Arithmetic Mean | Weighted Mean | Median Statistics |
|---|---|---|
| $\eta = 0.999 \pm 0.169$ | $\eta = 0.944 \pm 0.008$ | $\eta = 0.995 \pm 0.198$ |

to limit the transparency of the Universe (S. Cao & N. Liang 2011). In this analysis, a general parameterized form of CDDR is adopted, which can be expressed as

$$\eta(z) = \frac{D_L(z)}{D_A(z)(1+z)^2}, \tag{8}$$

where $D_L(z)$ and $D_A(z)$ represent the luminosity distance and angular diameter distance at the same redshift. In order to place constraints on the CDDR, it is necessary to determine both the luminosity distance and the angular diameter distance at the same redshift. One should expect $\eta(z) = 1$ at different redshifts to satisfy the validity of CDDR. In this paper, we present a new idea for testing Etherington's distance duality relation through the multiple measurements of CSOs. Their unique advantage lies in the fact that the *P–D* relation of CSOs involves both angular diameter distance and luminosity distance, thus reducing the systematical uncertainties suffered in the previous works (J.-P. Uzan et al. 2004; Z. Li et al. 2011; X. Zheng et al. 2020). Combining the reconstructed luminosity distance from SNe Ia and the angular diameter distance derived from the *P–D* relation, one can directly obtain the CDDR parameter $\eta(z)$ at different redshifts, without any prior assumption of its specific form. The corresponding measurements are displayed in Figure 9. One should emphasize that an accurate reconstruction of the CDDR parameter $\eta(z)$ may significantly improve our understanding of the cosmic acceleration (S. Geng et al. 2020). For instance, alternative theories can also explain this phenomenon, focusing on the absorption or scattering of photons by dust particles (such as cosmic opacity) (A. Avgoustidis et al. 2010). In our analysis, artificial neural network (ANN) method (G.-J. Wang et al. 2020) is applied to reconstruct the evolution of $\eta(z)$ with redshifts, by utilizing the code called reconstruct functions with ANN.[9] The reconstructed results are also presented in Figure 9. In order to quantify the deviation of the CDDR parameter from the standard case, we use three different statistical approaches (arithmetic mean, weighted mean, and median absolute deviation) to summarize the multiple $\eta(z)$ measurements (T. Liu et al. 2023). As is shown in Table 5, our findings indicate that no statistically significant evidence of deviation from the CDDR is detected from CSOs, being independent of any cosmological model. Our methodology produces stringent constraints on CDDR (with the precision of $10^{-3}$) at the current observational data level. Such precision is comparable to the previous CDDR analysis involving angular diameter distances from various astrophysical probes, i.e., BAOs (P. Wu et al. 2015), ultracompact radio quasars (J.-Z. Qi et al. 2019b), and strong gravitational lensing (L. Tang et al. 2025).

In conclusion, our analysis demonstrates that multiple measurements of CSOs reaching the redshifts $z \sim 0.8$ can be used as standard probes for cosmological inference. These findings have important implications for future CDDR tests with CSOs, i.e., our method would benefit substantially from expanded samples of high-redshift CSOs to better constrain the *P–D* relation, improved angular size measurements through next-generation VLBI observations, and a better understanding of systematic effects, particularly frequency-dependent position shifts.

[9] https://github.com/Guo-Jian-Wang/refann

## 5. Conclusions

In this paper, we revisit the dynamical model of hot spots proposed by M. Perucho & J. Martí (2003), in which the linear size and luminosity follow a simple power-law relation. However, the previous sample (M. Perucho & J. M. Marti 2002) exhibits a significant break between low and high-luminosity CSOs, which does not fit well with such a classic model. In this work, we use an updated CSO sample from archival VLBI data in both *S* and *X* bands (S. Kiehlmann et al. 2024), focusing on the subsample that exhibits edge brightening, high luminosity, and prominent hot spots (A. S. Readhead et al. 2024). The variation in hot spot separation speed with linear size follows an approximate power-law relation, with an exponent of $0.53 \pm 0.148$. The positive correlation we observe suggests that more powerful jets, which typically drive faster hot spot advancement, also tend to create larger-scale structures more rapidly. This observation provides strong support for self-similar evolution models of radio source development. We calibrate the CSO2.0 sample in a cosmology-model-independent manner using the reconstructed luminosity distance from the Pantheon+SH0ES SNe Ia sample (with the validity of CDDR) (D. Brout et al. 2022; A. G. Riess et al. 2022). The model parameters obtained in this analysis are generally in agreement with the simulation results (A. G. Sullivan et al. 2024). Meanwhile, we find that the angular separation size of CSOs varies across different frequencies, which cannot be explained solely by resolution difference (K. Sokolovsky et al. 2011). As the jet crosses the hot spots, it forms a backflow, causing high-energy particles to cool faster, which makes high-frequency emissions appear closer to the hot spots, while low-frequency emissions are closer to the core. Such a difference, simulated by the SPEV code (P. Mimica et al. 2010), is unable to fully reproduce the observed results. Furthermore, we calibrate 11 low-redshift sources in our CSO2.0 sample, using the reconstructed angular diameter distances from the cluster sample (without the assumption of CDDR) (E. De Filippis et al. 2005). This enables us to derive constraints on the hot spot dynamical model with different CSO samples, which are well consistent with those derived from the full CSO2.0 sample within $1\sigma$ C.L. Therefore, the density profile of the environment may be related to the redshift, which has important implications for understanding the interaction between young radio sources and their host galaxies.

In order to capture the overall trend and validate the hot spot dynamical model, we generate a simulated sample based on the semianalytical CSO model (A. G. Sullivan et al. 2024). We find that the relationship between luminosity and linear size is similar for both the existing sample and the simulated data. However, the hot spot radius may appear larger if the hot spot wiggles. Therefore, this model only provides a lower limit for the hot spot radius. This is well supported by the fitting results, where the intercepts in both the hot spot radius–luminosity and hot spot radius–linear size relationships are significantly smaller than those of the current sample, indicating that the model generally predicts a smaller hot spot radius compared to the current observations.

Finally, our analysis demonstrates that the *P–D* relationship of CSOs can be used as standard probes for cosmological inference, especially testing the CDDR. Considering the limited sample size of the current observations, we turn to the simulated sample generated by the semianalytical model. Our analysis demonstrates that CSOs can serve as valuable probes for testing fundamental physics. In particular, the CDDR parameter $\eta(z)$ could be directly obtained at different redshifts, without any prior assumption of its specific form. Our findings indicate that no statistically significant evidence of deviation from the CDDR is detected from CSOs, being independent of any cosmological model. One should be caution that the present paper is only the first step toward elaborating the scheme to calibrate CSOs as standard probes, taking advantage of multiple observations. Still, there are several remarks that remain to be clarified. First, such inference still heavily relies on the dynamical model of hot spots, which should be refined by incorporating magnetic field effects and detailed environmental interactions. Second, expanding the CSO sample across a wide redshift range is necessary. Both observations and theoretical models support that a fraction of CSOs are young radio sources, with a typical age of several hundred to several thousand years. Therefore, the *P–D* relation encodes the self-similar evolutionary process, rather than cosmological information, which allows the low-redshift *P–D* relation to be applied to the high-redshift range. We turn to an updated sample including CSOs, core jets, and CSO candidates (T. An et al. 2025), which exhibits a high degree of similarity with the sample of M. Perucho & J. M. Marti (2002). Moreover, since this sample has not yet undergone the CSO classification process (A. S. Readhead et al. 2024), we only exclude the CSO1 subsample, which has been explicitly identified (M. Perucho & J. M. Marti 2002). The resulting *P–D* relation agrees very well with the findings obtained in this work. In this aspect, follow-up work engaging multifrequency VLBI observations of more CSOs with higher sensitivity and angular resolution is desirable in the future.

## Acknowledgments

This work is supported by Beijing Natural Science Foundation No. 1242021, the National Natural Science Foundation of China (Nos. 12021003, 12433001, and 12041301), the National SKA Program of China (2022SKA0120102), the Strategic Priority Research Program of the Chinese Academy of Sciences, grant No. XDB23000000, the Interdisciplinary Research Funds of Beijing Normal University, and the Fundamental Research Funds for the Central Universities. We are grateful to the Astrogeo VLBI FITS image database for providing archival data from VLBA observations, which are crucial for our research.

## ORCID iDs

Yalong Nan https://orcid.org/0009-0003-0670-7189
Shuo Cao https://orcid.org/0000-0002-8870-981X
Tao An https://orcid.org/0000-0003-4341-0029
Haiyan Zhang https://orcid.org/0000-0003-1908-2408
Ailing Zeng https://orcid.org/0009-0000-9427-4608
Shiming Wen https://orcid.org/0009-0008-1361-4825

## References

An, T., & Baan, W. A. 2012, ApJ, 760, 77
An, T., Wu, F., Yang, J., et al. 2011, ApJS, 198, 5
An, T., Zhang, Y., Frey, S., Baan, W. A., & Wang, A. 2025, A&A, submitted (arXiv:2503.07288)
Avgoustidis, A., Burrage, C., Redondo, J., Verde, L., & Jimenez, R. 2010, JCAP, 2010, 024
Baan, W. A., & An, T. 2025, ApJ, 980, 119
Beasley, A., Gordon, D., Peck, A., et al. 2002, ApJS, 141, 13
Begelman, M. C. 1996, in Proc. of the Greenbank Workshop, Cygnus A: A Study of a Radio Galaxy, ed. C. L. Carilli & D. E. Harris (Cambridge: Cambridge Univ. Press), 209
Begelman, M. C., Blandford, R. D., & Rees, M. J. 1984, RvMP, 56, 255
Blandford, R., Meier, D., & Readhead, A. 2019, ARA&A, 57, 467
Bonamente, M., Joy, M. K., LaRoque, S. J., et al. 2006, ApJ, 647, 25
Branch, D., & Tammann, G. 1992, ARA&A, 30, 359
Bromberg, O., Nakar, E., Piran, T., et al. 2011, ApJ, 740, 100
Brout, D., Scolnic, D., Popovic, B., et al. 2022, ApJ, 938, 110
Cao, S., Biesiada, M., Jackson, J., et al. 2017a, JCAP, 2017, 012
Cao, S., Biesiada, M., Zheng, X., & Zhu, Z.-H. 2015, ApJ, 806, 66
Cao, S., Biesiada, M., Zheng, X., & Zhu, Z.-H. 2016, MNRAS, 457, 281
Cao, S., & Liang, N. 2011, RAA, 11, 1199
Cao, S., Qi, J., Biesiada, M., et al. 2019, PDU, 24, 100274
Cao, S., Zheng, X., Biesiada, M., et al. 2017b, A&A, 606, A15
Cao, S., & Zhu, Z. 2011, SCPMA, 54, 2260
Carvalho, J. 1994, A&A, 292, 392
Carvalho, J. C. 1998, A&A, 329, 845
Davis, R. A., Lii, K.-S., & Politis, D. N. 2011, Selected Works of Murray Rosenblatt (New York: Springer), 95
De Filippis, E., Sereno, M., Bautz, M. W., & Longo, G. 2005, ApJ, 625, 108
Etherington, I. M. H. 1933, PMag, 15, 761
Fanaroff, B. L., & Riley, J. M. 1974, MNRAS, 167, 31P
Fanti, C., Fanti, R., Dallacasa, D., et al. 1995, A&A, 302, 317
Fomalont, E., Frey, S., Paragi, Z., et al. 2000, ApJS, 131, 95
Fomalont, E., Petrov, L., MacMillan, D., Gordon, D., & Ma, C. 2003, AJ, 126, 2562
Geng, S., Cao, S., Liu, T., et al. 2020, ApJ, 905, 54
Gurvits, L. 1994, ApJ, 425, 442
Gurvits, L., Kellermann, K., & Frey, S. 1999, A&A, 342, 378
Hardcastle, M., & Croston, J. 2020, NewAR, 88, 101539
Helmboldt, J., Taylor, G., Tremblay, S., et al. 2007, ApJ, 658, 203
Hoyle, F., & Fowler, W. A. 1960, ApJ, 132, 565
Ishida, E. E., Reis, R. R., Toribio, A. V., & Waga, I. 2008, APh, 28, 547
Kaiser, C. R., & Alexander, P. 1997, MNRAS, 286, 215
Kardashev, N. S. 1962, SvA, 6, 317
Kellermann, K. I. 1993, Natur, 361, 134
Kiehlmann, S., Lister, M., Readhead, A. S., et al. 2024, ApJ, 961, 240
Kunert-Bajraszewska, M., Gawroński, M., Labiano, A., & Siemiginowska, A. 2010, MNRAS, 408, 2261
Lazkoz, R., Nesseris, S., & Perivolaropoulos, L. 2008, JCAP, 2008, 012
Lee, S.-S., Lobanov, A. P., Krichbaum, T. P., et al. 2008, AJ, 136, 159
Li, Z., Wu, P., & Yu, H. 2011, ApJL, 729, L14
Lister, M., Aller, H., Aller, M., et al. 2009, AJ, 137, 3718
Liu, T., Cao, S., Ma, S., et al. 2023, PhLB, 838, 137687
Liu, T., Cao, S., Zhang, S., et al. 2021, EPJC, 81, 903
Meier, D. L. 2012, Black Hole Astrophysics: the Engine Paradigm (Berlin: Springer)
Mimica, P., Giannios, D., & Aloy, M. 2010, MNRAS, 407, 2501
Murgia, M. 2003, PASA, 20, 19
Murgia, M., Fanti, C., Fanti, R., et al. 2002, NewAR, 46, 307
Nagai, H., Inoue, M., Asada, K., Kameno, S., & Doi, A. 2006, ApJ, 648, 148
Nakamura, M., Asada, K., Hada, K., et al. 2018, ApJ, 868, 146
O'Dea, C. P., & Baum, S. A. 1997, AJ, 113, 148
O'Dea, C. P., & Saikia, D. 2021, A&ARv, 29, 3
Parzen, E. 1962, Ann. Math. Statist., 33, 1065
Perucho, M., & Martí, J. 2003, PASA, 20, 94
Perucho, M., & Marti, J. M. 2002, ApJ, 568, 639
Perucho, M., Martí, J.-M., & Quilis, V. 2019, MNRAS, 482, 3718
Phillips, M. M. 1993, ApJL, 413, L105
Polatidis, A. G., & Conway, J. 2003, PASA, 20, 69
Qi, J.-Z., Cao, S., Zhang, S., et al. 2019a, MNRAS, 483, 1104
Qi, J.-Z., Cao, S., Zheng, C., et al. 2019b, PhRvD, 99, 063507
Qi, J.-Z., Zhao, J.-W., Cao, S., Biesiada, M., & Liu, Y. 2021, MNRAS, 503, 2179
Readhead, A., Cohen, M., Pearson, T., & Wilkinson, P. 1978, Natur, 276, 768
Readhead, A., Taylor, G., Pearson, T., & Wilkinson, P. 1996, ApJ, 460, 634
Readhead, A., Xu, W., Pearson, T., Wilkinson, P., & Polatidis, A. 1993, AAS Meeting, 182, 53.07
Readhead, A. S., Ravi, V., Blandford, R., et al. 2024, ApJ, 961, 242

Riess, A. G., Yuan, W., Macri, L. M., et al. 2022, ApJL, 934, L7
Risaliti, G., & Lusso, E. 2015, ApJ, 815, 33
Risaliti, G., & Lusso, E. 2019, NatAs, 3, 272
Samushia, L., & Ratra, B. 2009, ApJ, 703, 1904
Seikel, M., Clarkson, C., & Smith, M. 2012, JCAP, 2012, 036
Shepherd, M., Pearson, T., & Taylor, G. 1994, BAAS, 26, 987
Siemiginowska, A., Sobolewska, M., Migliori, G., et al. 2016, ApJ, 823, 57
Snellen, I., Schilizzi, R., & van Langevelde, H.-J. 2000, MNRAS, 319, 429
Sokolovsky, K., Kovalev, Y., Pushkarev, A., Mimica, P., & Perucho, M. 2011, A&A, 535, A24
Sullivan, A. G., Blandford, R. D., Begelman, M. C., Birkinshaw, M., & Readhead, A. C. 2024, MNRAS, 528, 6302
Tang, L., Lin, H.-N., & Wu, Y. 2025, ChPhC, 49, 015104
Taylor, G. B., Marr, J. M., Pearson, T. J., & Readhead, A. C. S. 2000, ApJ, 541, 112
Tengstrand, O., Guainazzi, M., Siemiginowska, A., et al. 2009, A&A, 501, 89
Tremblay, S., Taylor, G., Ortiz, A., et al. 2016, MNRAS, 459, 820
Urry, C. M., & Padovani, P. 1995, PASP, 107, 803
Uzan, J.-P., Aghanim, N., & Mellier, Y. 2004, PhRvD, 70, 083533
Petrov, L. 2018, The Astrogeo VLBI FITS image database, doi:10.25966/kyy8-yp57
Wang, G.-J., Ma, X.-J., Li, S.-Y., & Xia, J.-Q. 2020, ApJS, 246, 13
Wilkinson, P., Polatidis, A., Readhead, A., Xu, W., & Pearson, T. 1994, ApJL, 432, L87
Wu, P., Li, Z., Liu, X., & Yu, H. 2015, PhRvD, 92, 023520
Zheng, X., Liao, K., Biesiada, M., et al. 2020, ApJ, 892, 103